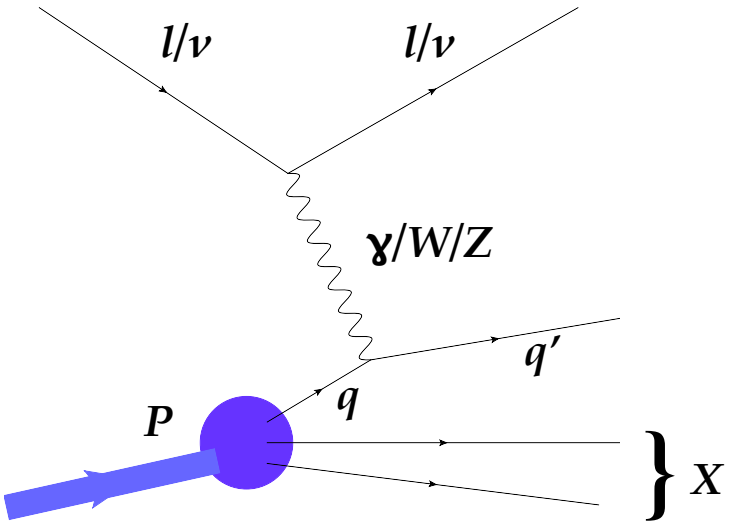

Figure 1: Schematic representation of the deep-inelastic scattering process. An energetic lepton (electron, muon or neutrino) scatters off one of the quarks in the proton by means of the interchange of a gauge boson ($\gamma, W^{\pm}$ or Z). The large virtuality of the gauge boson, $Q \gg \Lambda_{\rm QCD}$, ensures that the process can be described within QCD factorization in terms of coefficient functions and parton distributions.

1. From the authors

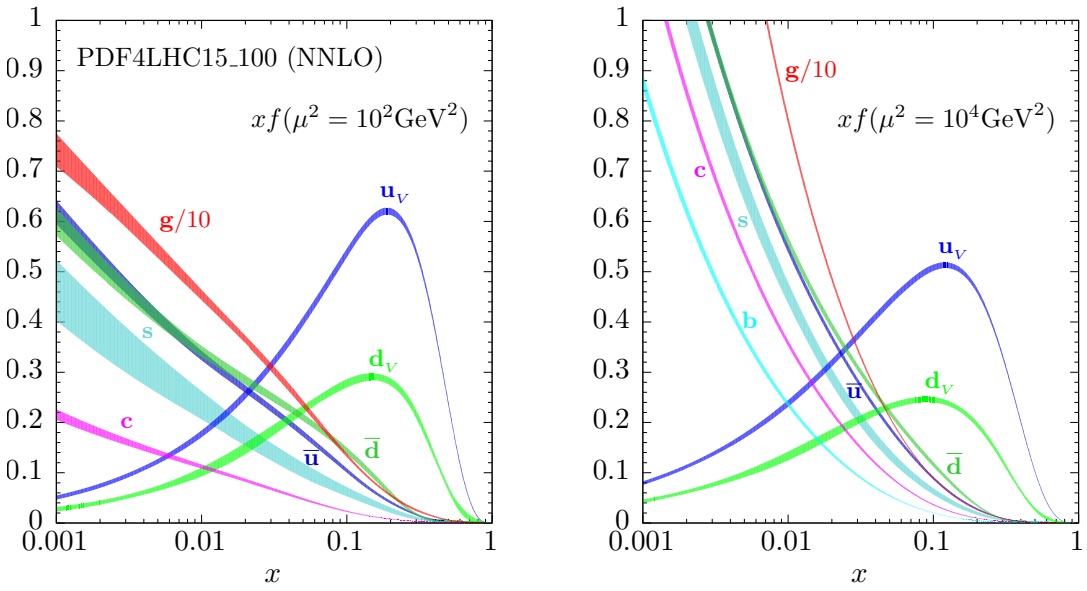

Figure 2: The effect of the DGLAP evolution in the PDF4LHC NNLO Hessian set (with 100 eigenvectors), comparing the PDFs at a low scale of $Q^2 = 10$ GeV^2 (left) with the same PDFs evolved up to a typical LHC scale of $Q^2 = 10^4$ GeV^2 (right plot). In this plot the PDFs are shown together with the corresponding one-sigma PDF uncertainty band.

2. From the authors

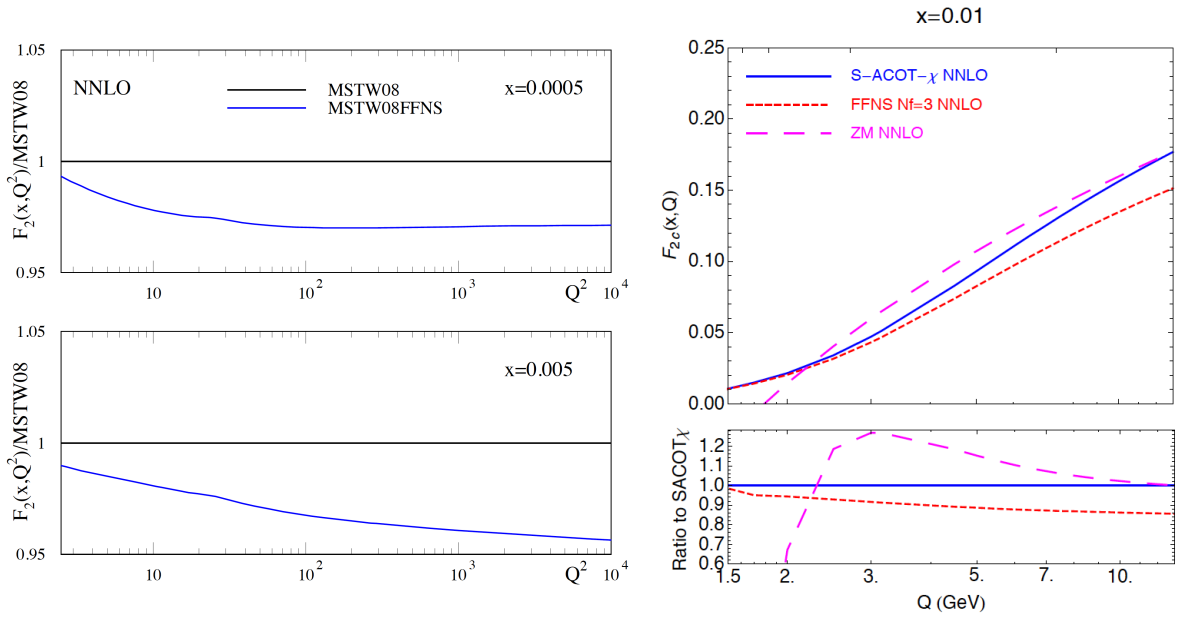

Figure 3: Left plot: the inclusive proton structure function $F_2^2(x, Q^2)$ at NNLO as a function of Q^2 for two different values of x in the RT' GM-VFNS as compared to the FFNS calculation. Right plot: the NNLO charm structure function $F_2^c(x, Q)$ as a function of Q for $x = 0.01$ comparing the S-ACOT-χ GM scheme with the corresponding ZM and FFN scheme calculations.

3. From Left: R. Thorne, The effect on PDFs and S (MZ2) due to changes in flavour scheme and higher twist contributions, Eur.Phys.J. C74 (7) (2014) 2958. arXiv:1402.3536; Right: M. Guzzi, P. M. Nadolsky, H.-L. Lai, C.-P. Yuan, General-Mass Treatment for Deep Inelastic Scattering at Two-Loop Accuracy, Phys.Rev. D86 (2012) 053005

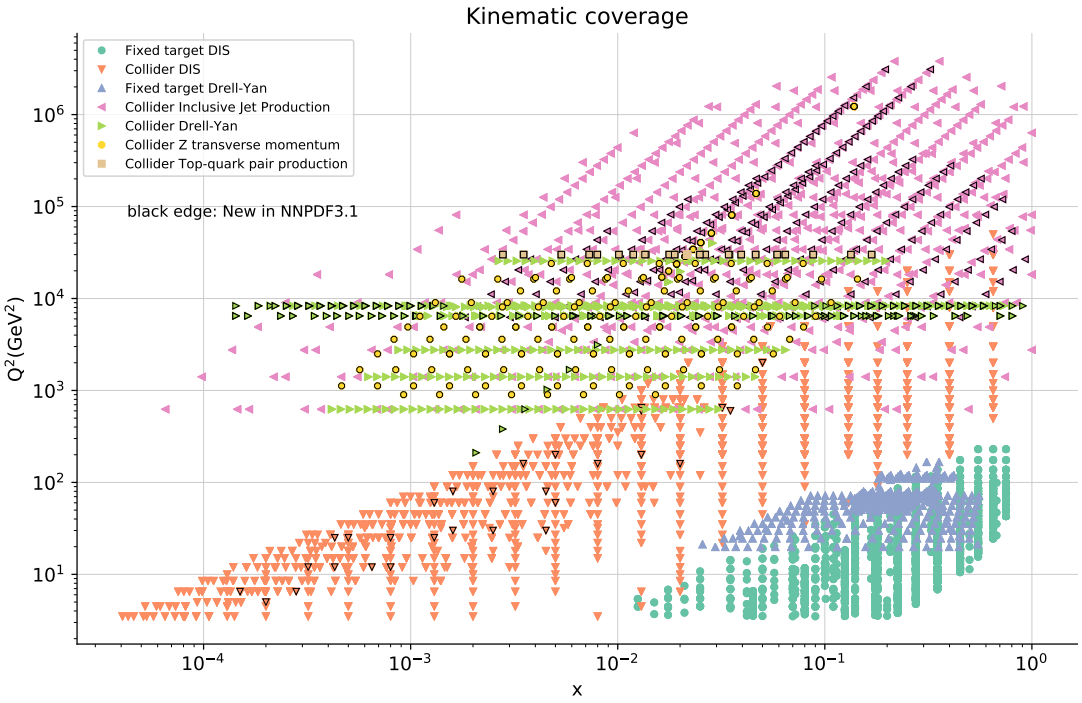

Figure 4: Typical kinematical coverage in the (x, Q^2) plane for the dataset included in a global analysis, in this case NNPDF3.1. For hadronic observables, leading order kinematics are assumed to map each data bin to a pair of (x, Q^2) values. The various datasets are clustered into families of related processes.

4. From R. D. Ball, et al., Parton distributions from high-precision collider dataarXiv:1706.00428

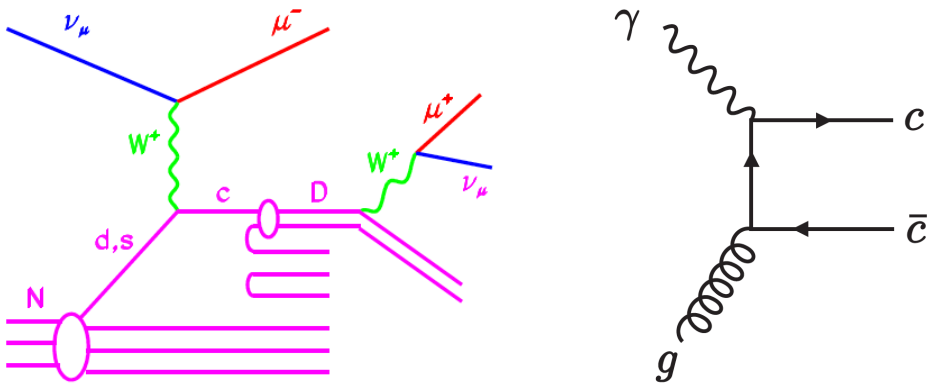

Figure 5: Left plot: D meson production in charged-current neutrino-induced DIS. This is known as the dimuon process since events are tagged where the D meson decays semi-leptonically, with the pair of oppositely charged muons providing a clean signature. Right plot: Charm production in neutral current DIS at leading order, highlighting the sensitivity of this process to the gluon PDF.

5. From the authors

6. From Left: J. Currie, E. W. N. Glover, A. Gehrmann-De Ridder, T. Gehrmann, A. Huss, J. Pires, Single jet inclusive production for the individual jet pT scale choice at the LHC, in: 23rd Cracow Epiphany Conference on Particle Theory Meets the First Data from LHC Run 2 Cracow, Poland, January 9-12, 2017, 2017. arXiv:1704.00923; Right: the authors

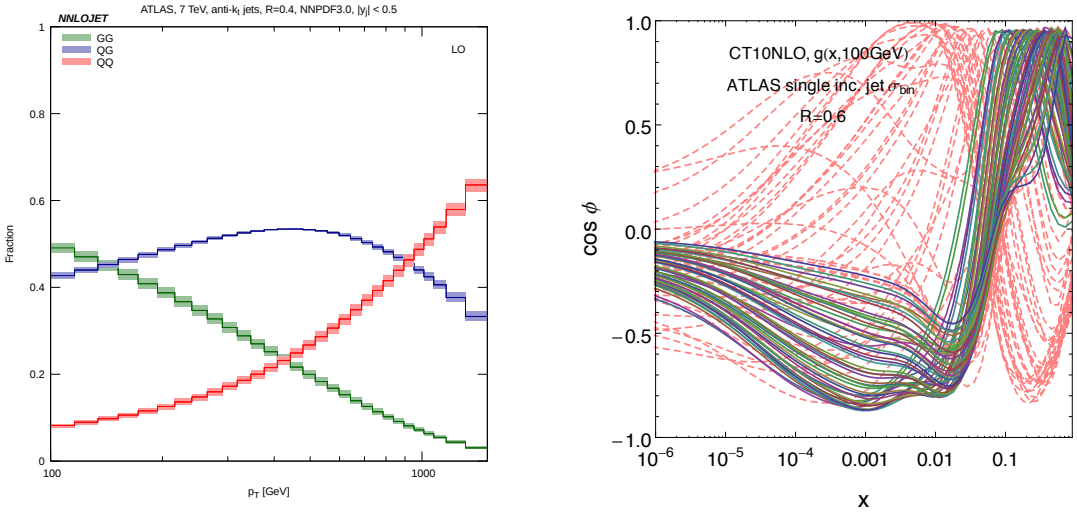

Figure 6: Left: Fractional contributions from different partonic channels to the single inclusive jet production at the LHC 7 TeV at LO in the central rapidity region [**?**]. Right: Correlations between binning cross sections from ATLAS on the single inclusive jet production at the LHC 7 TeV and the gluon PDF; dashed curves correspond to experiment bins at low p_T.

7. From Left: G. Aad, et al., Measurement of the inclusive jet cross-section in proton-proton collisions at s = 7 TeV using 4.5 fb1 of data with the ATLAS detector, JHEP 02 (2015) 153, [Erratum: JHEP09,141(2015)]. arXiv:1410.8857, doi:10.1007/JHEP02(2015)153, 10.1007/JHEP09(2015)141; Right: S. Chatrchyan, et al., Measurement of the ratio of inclusive jet cross sections using the anti-kT algorithm with ra- dius parameters R=0.5 and 0.7 in pp collisions at s = 7TeV, Phys. Rev. D90 (7) (2014) 072006. arXiv:1406.0324, doi:10.1103/PhysRevD.90.072006

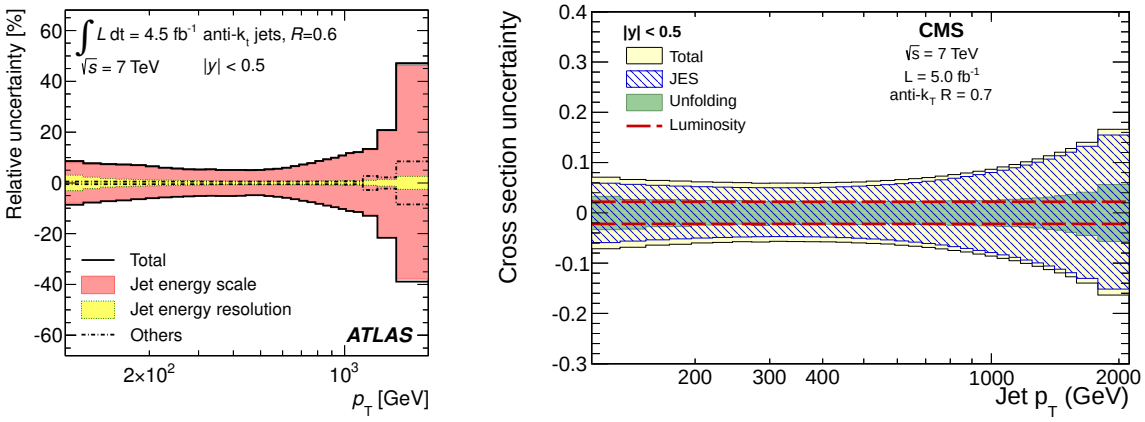

Figure 7: Representative systematic errors in single inclusive jet measurement at LHC 7 TeV in the central rapidity region, from ATLAS (left) [**?**] and CMS (right) [**?**]. The luminosity error is not included in the ATLAS plot.

8. From J. Currie, E. W. N. Glover, A. Gehrmann-De Ridder, T. Gehrmann, A. Huss, J. Pires, Single jet inclusive production for the individual jet pT scale choice at the LHC, in: 23rd Cracow Epiphany Conference on Particle Theory Meets the First Data from LHC Run 2 Cracow, Poland, January 9-12, 2017, 2017. arXiv:1704.00923

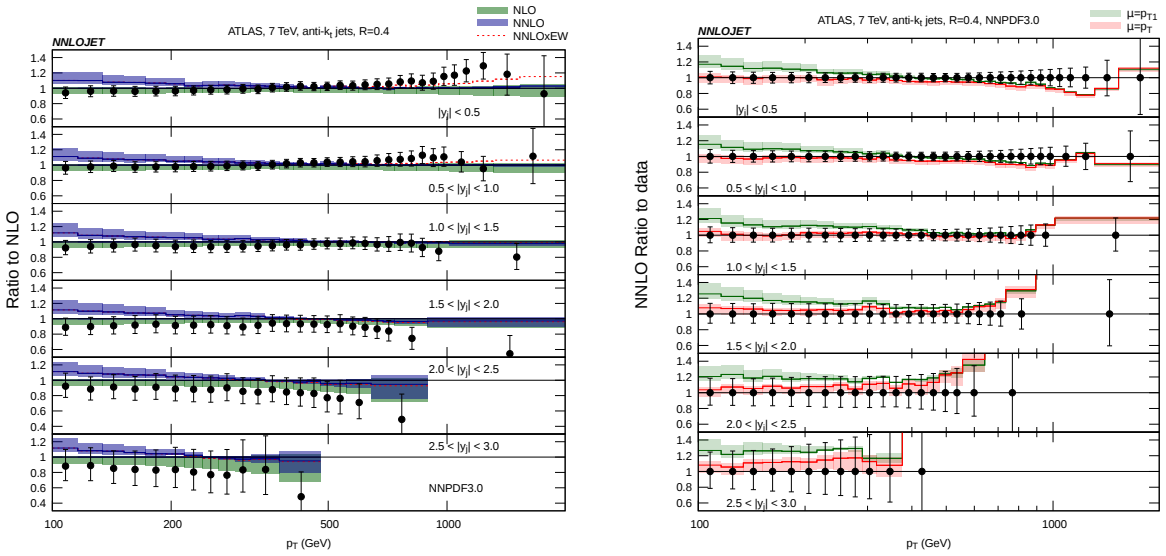

Figure 8: Left: Predictions on single inclusive jet production at the LHC 7 TeV using ATLAS binning and anti-k_T algorithm with $R = 0.4$, with a central scale choice of leading jet p_T and scale variations by varying renormalization and factorization scales simultaneously by a factor of 2 [**?**]. Right: For the same setup comparing the NNLO predictions using a central scale choice of the leading jet p_T (green) and the individual jet p_T (red) [**?**].

9. From A. M. Sirunyan, et al., Measurement of the triple-differential dijet cross section in proton-proton collisions at sqrt(s) = 8 TeV and constraints on parton distribution functionsarXiv:1705.02628

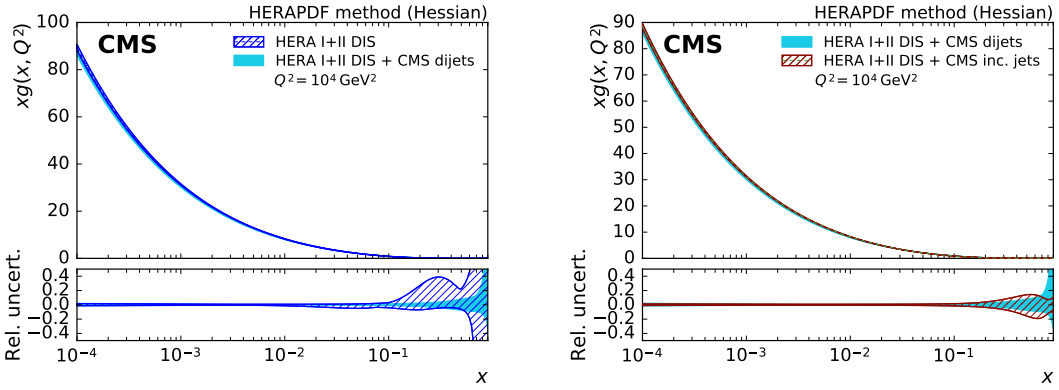

Figure 9: Effects of the CMS 8 TeV jet data on the gluon PDF when adding up to a PDF fit with HERA DIS data only. The left plot compares the fit with only DIS data and the fit with CMS dijet data in addition. The right plot compares the fit to HERA DIS plus CMS dijet data and fit to HERA DIS plus CMS single jet data [**?**].

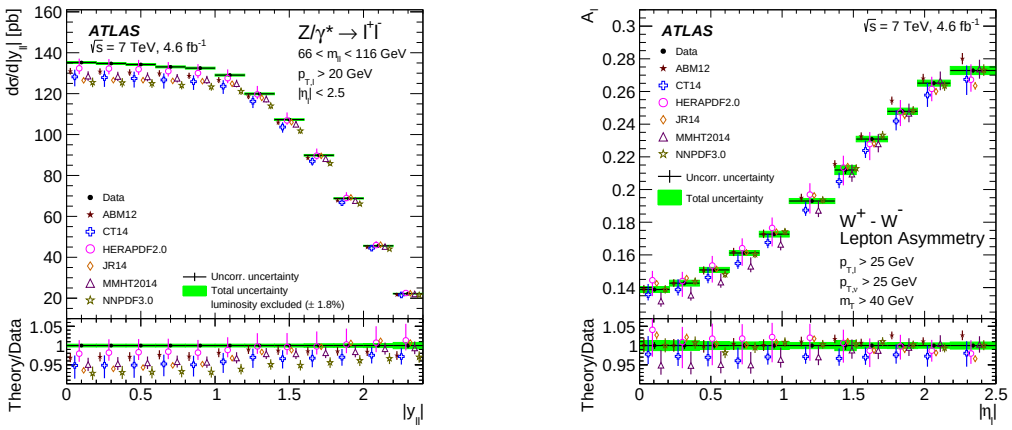

Figure 10: ATLAS 7 TeV measurement of Z rapidity distribution (left) and W asymmetry (right), taken from [**?**].

10. From M. Aaboud, et al., Precision measurement and interpretation of inclusive W+, W and Z/ production cross sections with the ATLAS detectorarXiv:1612.03016

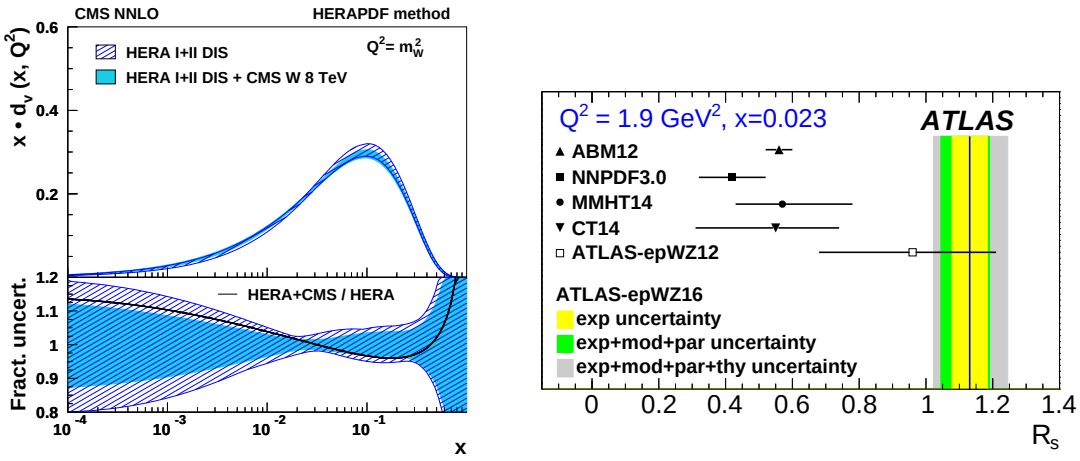

Figure 11: (Left) Down valence distribution, with the CMS fit to HERA I+II data only, and including the CMS 8 TeV W production data. Taken from [**?**]. (Right) The ratio of the strange quark to the light quark sea, R_s, with different PDF predictions and the result of the ATLAS fit to HERA I+II data and the high precision W and Z/γ^* data shown. Taken from [**?**].

11. From Left: V. Khachatryan, et al., Measurement of the differential cross section and charge asymmetry for inclusive pp W + X production at s = 8 TeV, Eur. Phys. J. C76 (8) (2016) 469. arXiv:1603.01803; Right: M. Aaboud, et al., Precision measurement and interpretation of inclusive W+, W and Z/ production cross sections with the ATLAS detectorarXiv:1612.03016

12. From R. Boughezal, A. Guffanti, F. Petriello, M. Ubiali, The impact of the LHC Z-boson transverse momentum data on PDF determinations, JHEP 07 (2017) 130. arXiv:1705.00343, doi:10.1007/JHEP07(2017)130

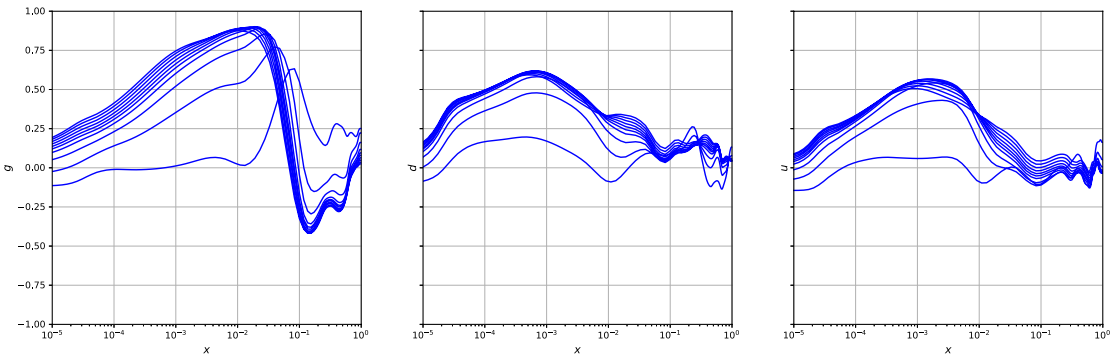

Figure 12: Correlations between the cross sections in various p_T bins and the gluon, down- and up-quark PDFs as a function of x [**?**]. The binning corresponds to the ATLAS measurement [**?**] with rapidity interval $0 < |y_Z| < 0.4$.

13. From Left:G. Aad, et al., Measurement of the transverse momentum and distributions of DrellYan lepton pairs in proton- proton collisions at s = 8 TeV with the ATLAS detector, Eur. Phys. J. C76 (5) (2016) 291; Right: V. Khachatryan, et al., Measurement of the Z boson differential cross section in transverse momentum and rapidity in protonproton collisions at 8 TeV, Phys. Lett. B749 (2015) 187209. arXiv:1504.03511

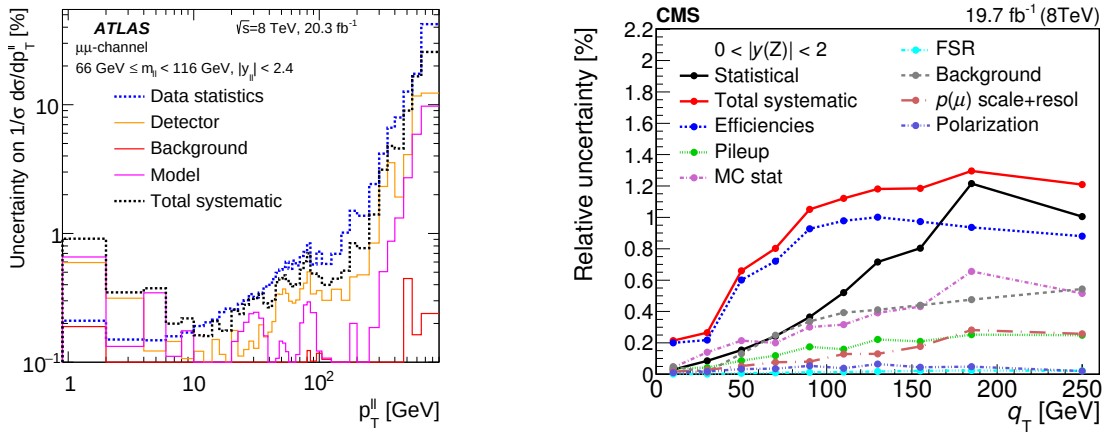

Figure 13: Left plot: relative experimental errors on the measured normalized p_T spectra of the Z boson in dimuon channel (dressed) from ATLAS 8 TeV [**?**] . Right plot: relative experimental errors on the measured normalized p_T spectra of the Z boson in dimuon channel from CMS 8 TeV [**?**] .

14. From A. Gehrmann-De Ridder, T. Gehrmann, E. W. N. Glover, A. Huss, T. A. Morgan, NNLO QCD corrections for Drell-Yan pZT and observables at the LHC, JHEP 11 (2016) 094. arXiv:1610.01843

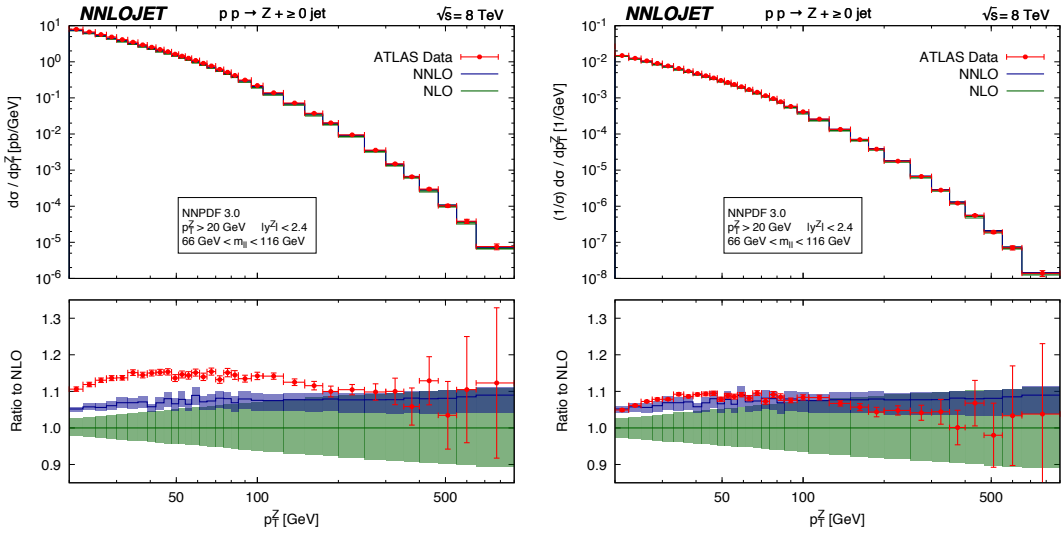

Figure 14: Left(right) plot shows the unnormalized(normalized) transverse momentum distribution of the inclusive Z boson production at LHC 8 TeV [**?**]. The green and blue bands denote the NLO and NNLO predictions with scale variations. The fiducial cuts on charged leptons are $p_{T,l} > 20\,\mathrm{GeV}$ and $|\eta_l| < 2.4$.

15. From R. D. Ball, et al., Parton distributions from high-precision collider dataarXiv:1706.00428

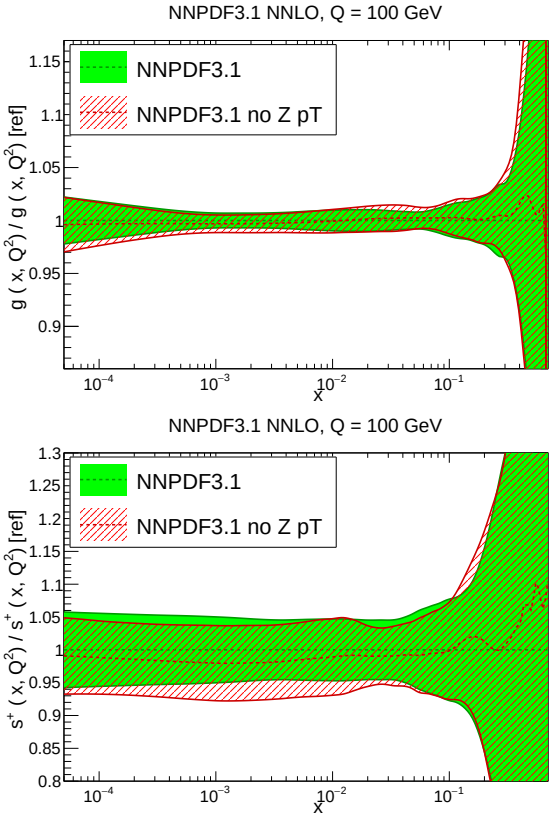

Figure 15: Impact of the Z boson transverse momentum measurements from ATLAS and CMS 8 TeV on the gluon PDF and the total strangeness in the NNPDF3.1 global analyses [**?**].

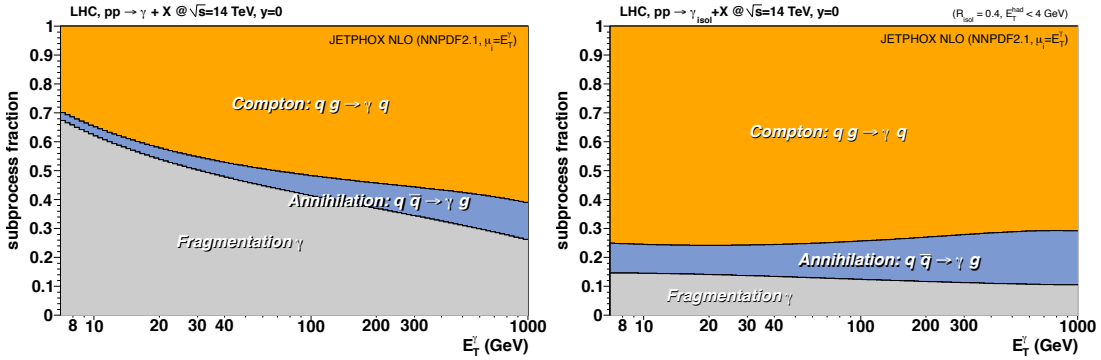

Figure 16: Relative contributions from Compton (qg), annihilation ($q\overline{q}$) and fragmentation to prompt photon production at central rapidities at the 14 TeV LHC, before (left) and after (right) the application of isolation cuts. Figures taken from [**?**].

16. From D. dEnterria, J. Rojo, Quantitative constraints on the gluon distribution function in the proton from collider isolated-photon data, Nucl.Phys. B860 (2012) 311338. arXiv:1202.1762

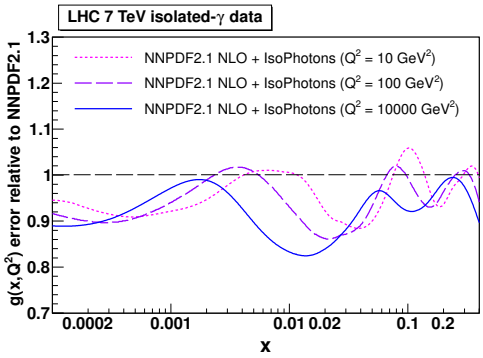

Figure 17: Relative reduction in the NNPDF2.1 NLO gluon PDF uncertainty when including a 36 pb^{-1} LHC 7 TeV isolated photon data set via reweighting. Taken from [**?**].

17. From D. dEnterria, J. Rojo, Quantitative constraints on the gluon distribution function in the proton from collider isolated-photon data, Nucl.Phys. B860 (2012) 311338. arXiv:1202.1762

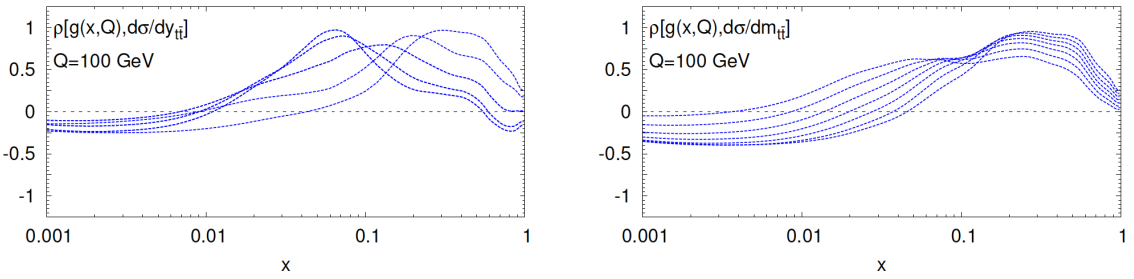

Figure 18: The correlation coefficient between the gluon PDF at $Q = 100$ GeV and the theory predictions for the differential distributions in $y_{t\bar{t}}$ (left) and $m_{t\bar{t}}$ (right plot) at $\sqrt{s} = 8$ TeV, as a function of x. Each curve corresponds to a specific measurement bin. The higher the absolute value of the correlation coefficient, the bigger the sensitivity to the gluon in those specific values of x.

18. From the authors

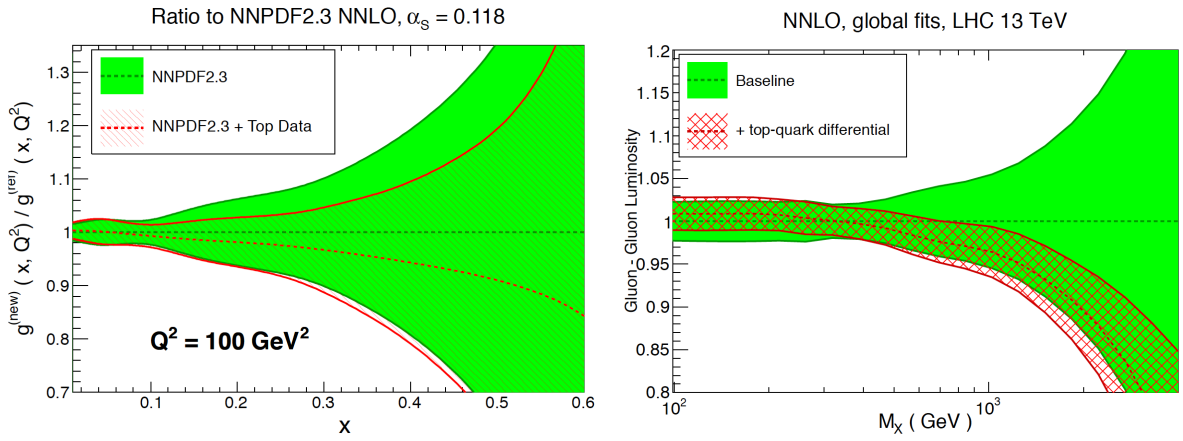

Figure 19: Left plot: the impact of the LHC 7 and 8 TeV inclusive top-quark pair cross-section data on the large-x gluon of NNPDF2.3 [**?**]. Right plot: the impact of the LHC 8 TeV differential distributions in top-quark pair production on the gg luminosity [**?**], compared with a baseline fit based on the NNPDF3.0 global analysis without the jet data.

19. From Left: M. Czakon, M. L. Mangano, A. Mitov, J. Rojo, Constraints on the gluon PDF from top quark pair production at hadron colliders, JHEP 1307 (2013) 167. arXiv:1303.7215; Right: M. Czakon, N. P. Hartland, A. Mitov, E. R. Nocera, J. Rojo, Pinning down the large-x gluon with NNLO top-quark pair differential distributions, JHEP 04 (2017) 044. arXiv:1611.08609

20. From Left: the authors; Right: M. Aaboud, et al., Measurement of the inclusive cross-sections of single top-quark and top-antiquark t-channel pro- duction in pp collisions at s = 13 TeV with the ATLAS detector, JHEP 04 (2017) 086. arXiv:1609.03920

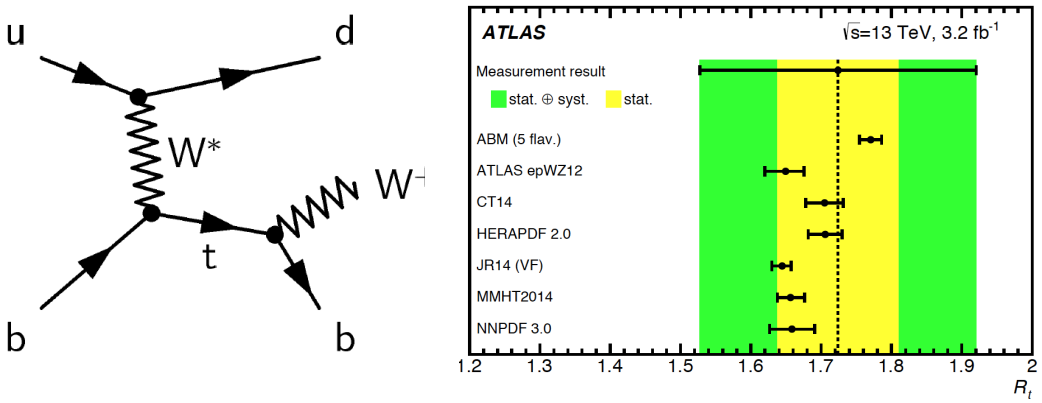

Figure 20: Left plot: one of the Feynman diagrams for single-top production at leading order, illustrating its sensitivity to the b-quark PDF. Right plot: comparison of the theoretical predictions for the ratio $R_t = \sigma_t/\sigma_{\bar{t}}$ from different PDF sets and the corresponding ATLAS measurements at $\sqrt{s} = 13$ TeV from [**?**].

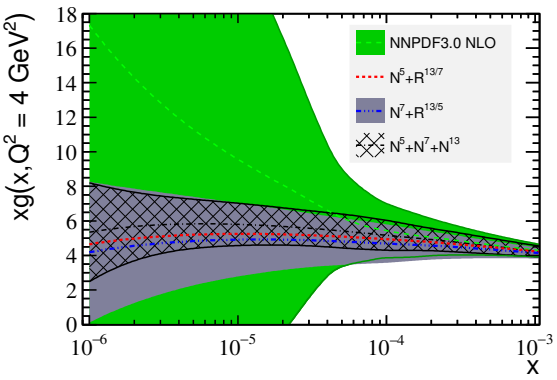

Figure 21: Left plot: comparison between the small-x gluon at $Q^2 = 4$ GeV^2 in NNPDF3.0 with the corresponding result after different combinations of the charm production data at LHCb have been included in the fit. We show the central value and one-sigma PDF uncertainty bands for the $N^7 + N^{13/5}$ and the $N^5 + N^7 + N^{13}$ combinations, as well as the central value for the $N^5 + N^{13/7}$ case

21. From the authors

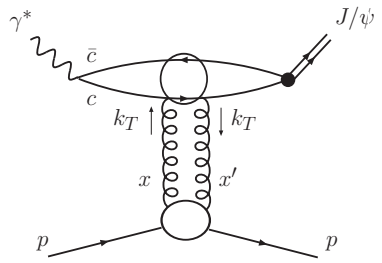

Figure 22: Figure from 1307.7099. **perhaps don't need a figure- if we decide to keep, will find better one...**

22. From arXiv:1307.7099

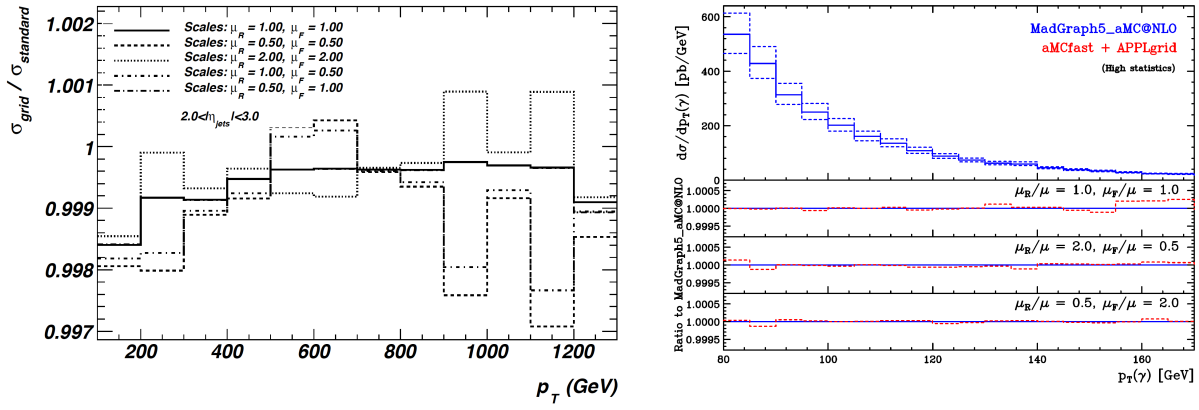

Figure 23: Right plot: the ratio between the `NLOjet++` calculation of inclusive jet production at 7 TeV in the rapidity interval $2 \leq y \leq 3$ and the corresponding *a posteriori* calculation based on `APPLgrid`, for different values of the factorization and renormalization scales. Left plot: the transverse momentum distribution of photons in the $pp \to \gamma + \text{jet}$ process at 7 TeV, comparing the original `MadGraph5_aMC@NLO` calculation with the *a posteriori* result based on `aMCfast` and `APPLgrid`. The lower insets show the ratio between the two calculations for different choices of μ_R and μ_F.

23. From the authors

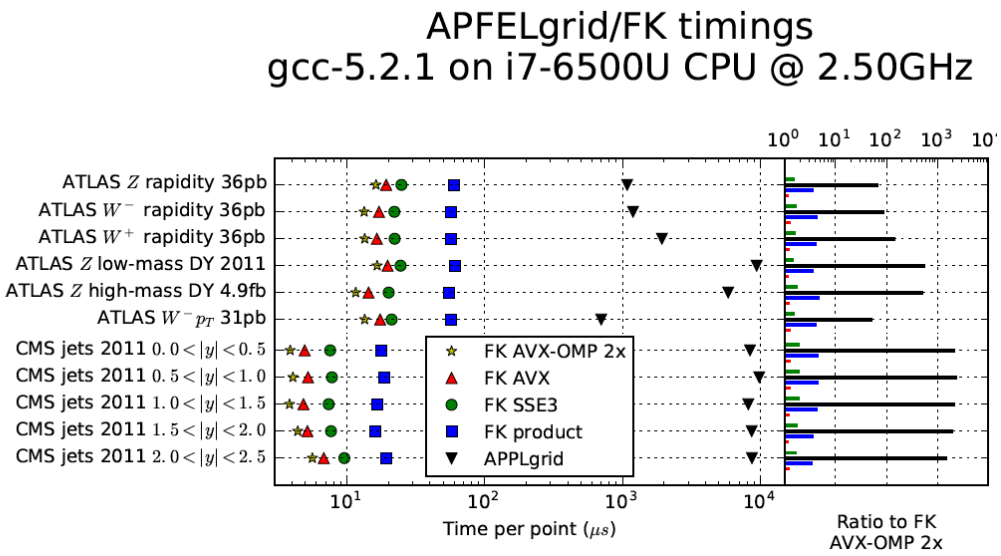

Figure 24: Comparison of the timings per data point between the original `APPLgrid` computation of hadronic cross-sections, Eq. (**??**), with the same calculation based on the `APFELgrid` combination, Eq. (**??**), for a variety of LHC datasets. We find that the improvement in computational speed is between a factor 100 and a factor 1000 depending on the specific dataset.

24. From the authors

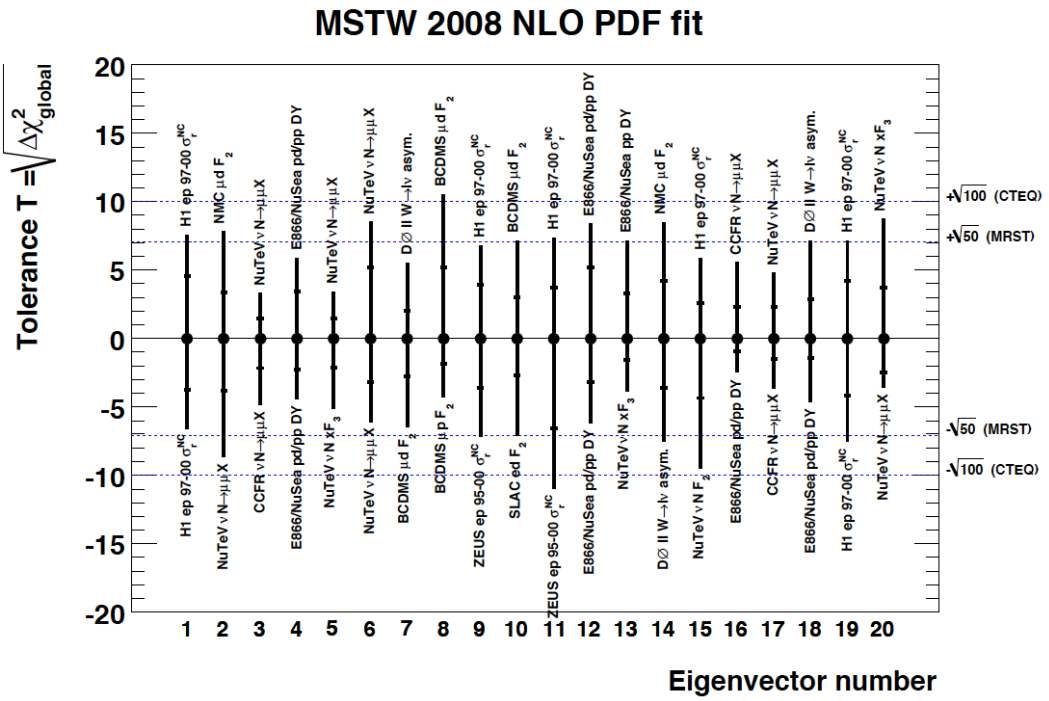

Figure 25: The individual tolerance for each eigenvector, determined by the criterion that each separate experiment should be described within 90% CL. In each case the figure indicates the name of the experiment that determines the tolerance for the various eigenvector directions.

25. From A. D. Martin, W. J. Stirling, R. S. Thorne, G. Watt, Parton distributions for the LHC, Eur. Phys. J. C63 (2009) 189. arXiv:0901.0002

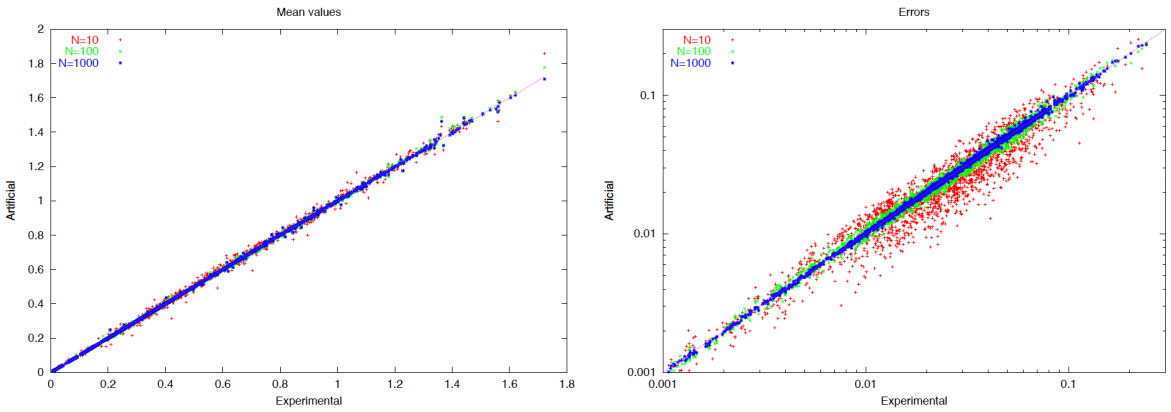

Figure 26: The scatter between the mean values (left) and variances (right plot) of all the data points included in the analysis of [**?**], comparing the original experimental values with the results obtained from the MC representation for different number $N_{\rm rep}$ of replicas.

26. From L. Del Debbio, S. Forte, J. I. Latorre, A. Piccione, J. Rojo, Unbiased determination of the proton structure function f2(p) with estimation, JHEP 03 (2005) 080. arXiv:hep-ph/0501067

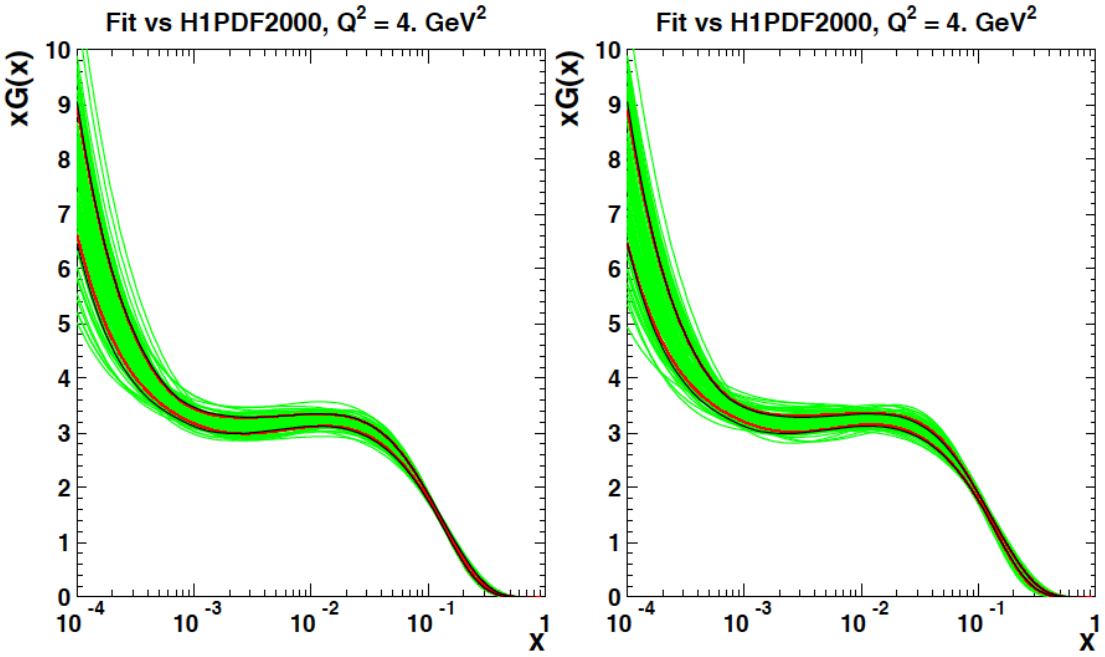

Figure 27: The gluon PDF at $Q = 2$ GeV in the HERA-LHC benchmark fit of Ref. [**?**], where the one-sigma PDF uncertainties computed with the Hessian method (black lines) are compared to those of the Monte Carlo method (red lines), finding good agreement. Each of the green curves corresponds to an individual MC replica. In the left fit, the normalization and systematic uncertainties in the MC replicas from Eq. (**??**) fluctuate according to a multi-Gaussian distribution, while in the right fit they fluctuate instead according to a log-normal distribution.

27. From M. Dittmar, et al., Parton Distributions, arXiv:0901.2504

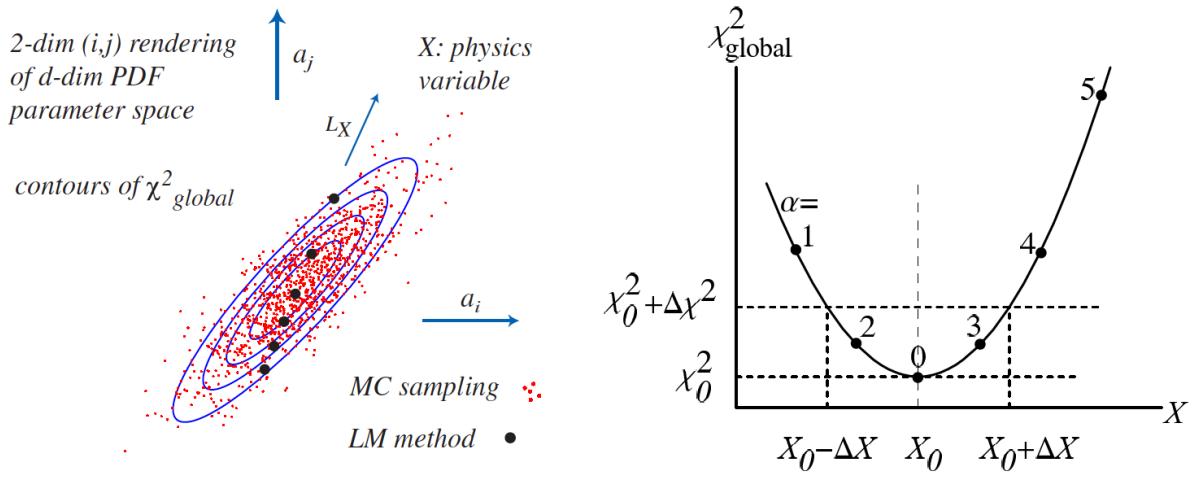

Figure 28: Schematic representation of the Lagrange Multiplier method. In the left plot we show a two-dimensional projection of the PDF parameter space, indicating the contours in χ^2 for fixed values of the physical quantity $\mathcal{F}$. In the right plot we show how the PDF uncertainty associated to $\mathcal{F}$ for a given confidence interval is determined by the condition that the global χ^2 should not grow beyond the tolerance $\Delta\chi^2$.

28. From the authors

29. From Left: L. A. Harland-Lang, A. D. Martin, P. Motylinski, R. S. Thorne, Uncertainties on S in the MMHT2014 global PDF analysis and implications for SM predictionsarXiv:1506.05682; Right: R. D. Ball, V. Bertone, L. Del Debbio, S. Forte, A. Guffanti, et al., Precision NNLO determination of s(MZ) using an unbiased global parton set, Phys.Lett. B707 (2012) 6671. arXiv:1110.2483

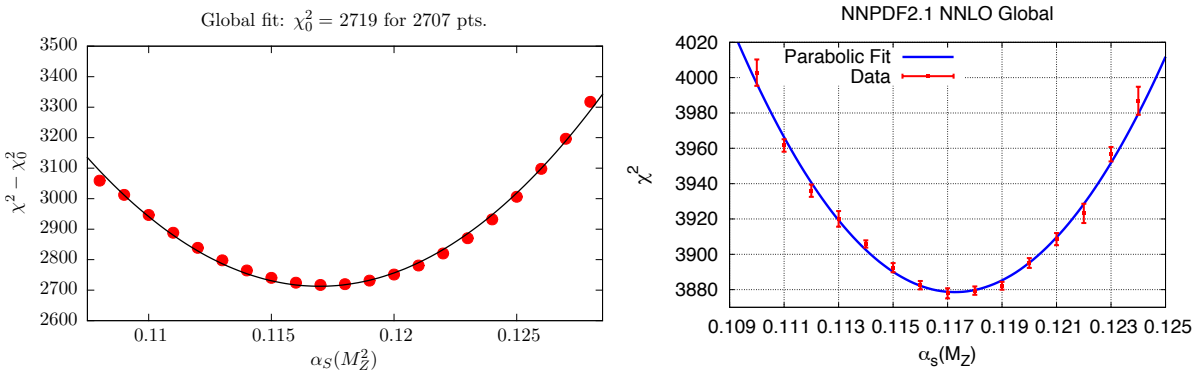

Figure 29: Left plot: the profile of global χ^2 as in a scan of $\alpha_s(M_Z)$ in MMHT2014 NNLO analysis [**?**]. Right plot: the profile of global χ^2 as in a scan of $\alpha_s(M_Z)$ in NNPDF2.1 NNLO analysis [**?**]. The error bars indicate fluctuations of the χ^2 due to finite number of MC replicas.

30. From H.-L. Lai, et al., Uncertainty induced by QCD coupling in the CTEQ global analysis of parton distributions, Phys. Rev. D82 (2010) 054021. arXiv:1004.4624

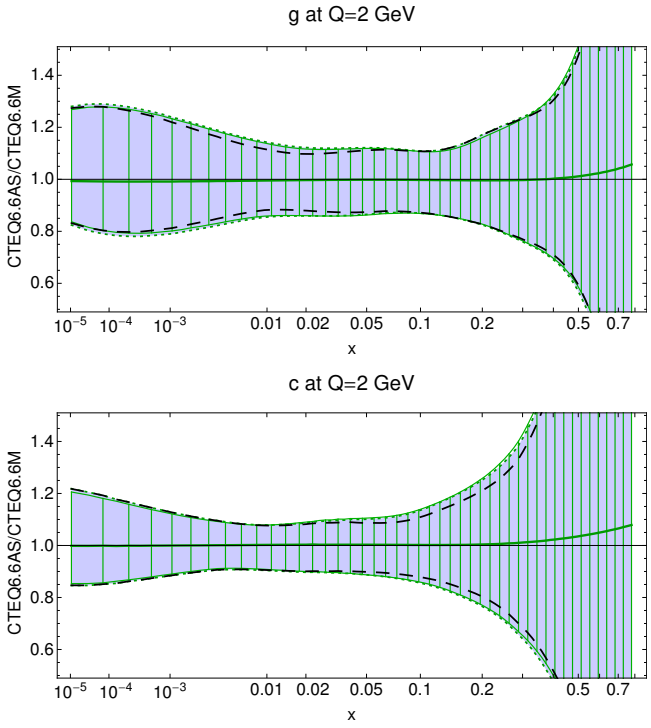

Figure 30: Comparison of the PDF+α_s uncertainties for gluon and charm quark PDFs as from the full eigenvectors including $\alpha_s(M_Z)$ in the Hessian matrix (filled error band with dotted borders) and the seperate PDF and α_s uncertainties added in quadrature (hatched band with solid borders) [**?**]. The dashed lines represent the PDF uncertianties only.

31. From T.-J. Hou, S. Dulat, J. Gao, M. Guzzi, J. Huston, P. Nadolsky, C. Schmidt, J. Winter, K. Xie, C. P. Yuan, CT14 Intrinsic Charm Parton Distribution Functions from CTEQ-TEA Global AnalysisarXiv:1707.00657.

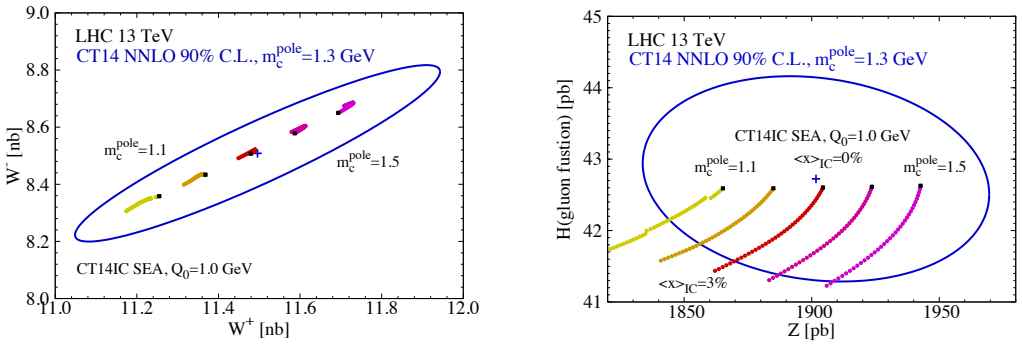

Figure 31: Dependence of total cross sections of weak boson and Higgs boson productions at LHC 13 TeV on the choice of charm quark mass in CT14 NNLO analysis [**?**]. The ellipse indicates PDF uncertainties at 90% C.L. Also shown are dependence of the cross sections on the assumed momentum fraction carried by non-perturbative charm PDF at the initial scale.

32. From J. Butterworth, et al., PDF4LHC recommendations for LHC Run II, J. Phys. G43 (2016) 023001. arXiv:1510.03865

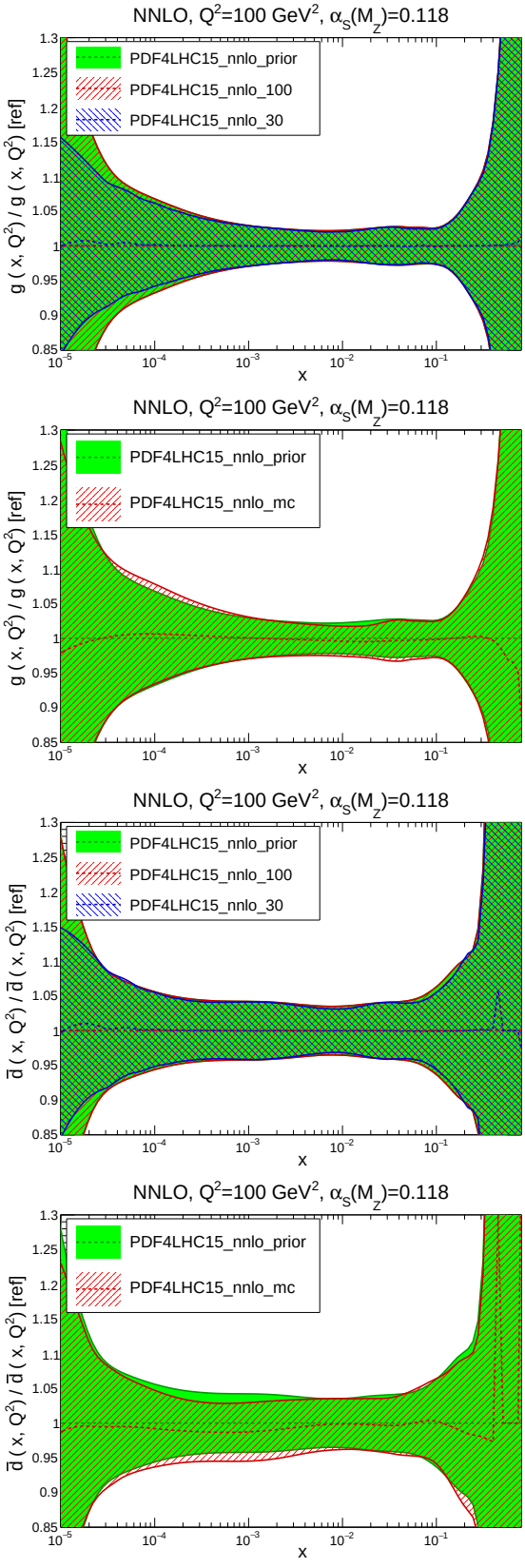

Figure 32: Comparison of the gluon and $\bar{d}$-quark PDFs at a scale of $Q^2 = 100\,\mathrm{GeV}^2$ between the prior and the two reduced Hessian sets, and between the prior and the compressed MC set, normalized to the central value of the prior [**?**].

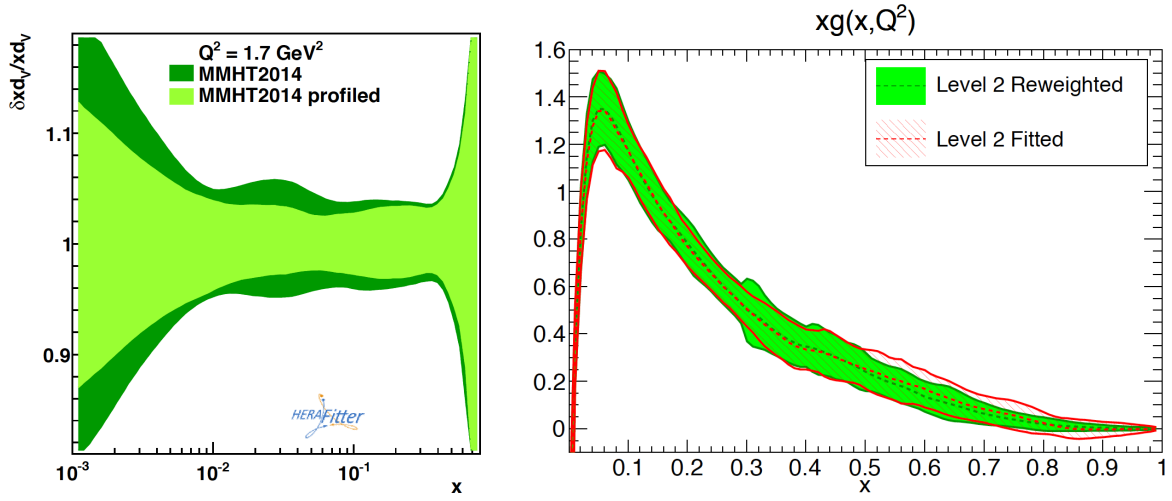

Figure 33: Left plot: the impact of the Tevatron W and Z data on the MMHT2014 NLO fit, estimated by the Hessian profiling method of Ref. [**?**]. Right plot: the gluon PDF in the NNPDF3.0 closure tests, quantifying the impact of the collider inclusive jet data, and comparing the results of the Bayesian reweighting with those of a direct refit.

33. From Left: S. Camarda, et al., QCD analysis of W- and Z-boson production at Tevatron, Eur. Phys. J. C75 (9) (2015) 458. arXiv:1503.05221; Right: the authors

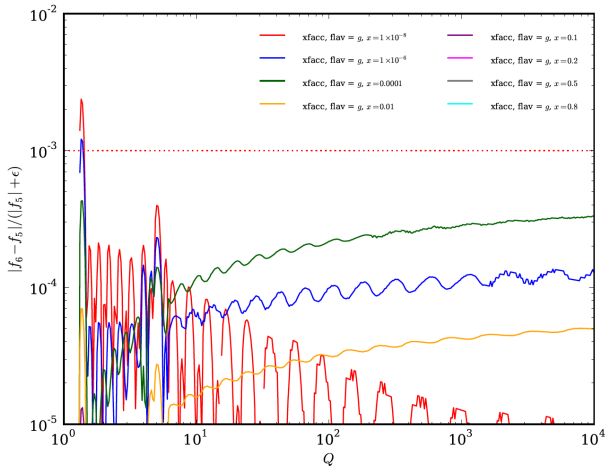

Process/PDF	t_5	t_6	t_5/t_6
Cross-section integrations, 1M phase space points			
CT10			
$pp \to jj$	23'10"	9'17"	2.5
$pp \to \ell\ell$	4'12"	2'02"	2.1
$pp \to H$ (ggF)	0'20"	0'15"	1.3
NNPDF23nlo			
$pp \to jj$	54'40"	9'28"	5.8
$pp \to \ell\ell$	8'06"	2'33"	3.2
$pp \to H$ (ggF)	0'25"	0'11"	2.3
CKKW event generation, 100k $pp \to \leq 4$ jet events			
CT10			
Weighted	43'02"	35'47"	1.2
Unweighted	5h04'39"	4h30'26"	1.1
NNPDF23nlo			
Weighted	47'47"	27'20"	1.7
Unweighted	6h44'47"	4h48'26"	1.4

Figure 34: Left plot: the relative difference between LHAPDF v5 and v6 for $g(x, Q)$ for different values of x as a function of Q, using CT10 as input PDF. Right plot: the timing improvement in v6 as compared to v5, t_6/t_5, for a cross-section integration of 1M phase space points with `Sherpa` and for CKKW event generation of 100k $pp \to 4$ jet events.

34. From A. Buckley, J. Ferrando, S. Lloyd, K. Nordstrm, B. Page, et al., LHAPDF6: parton density access in the LHC precision era, Eur.Phys.J. C75 (2015) 132. arXiv:1412.7420

35. From S. Dulat, T.-J. Hou, J. Gao, M. Guzzi, J. Huston, P. Nadolsky, J. Pumplin, C. Schmidt, D. Stump, C. P. Yuan, New parton distribution functions from a global analysis of quantum chromodynamics, Phys. Rev. D93 (3) (2016) 033006

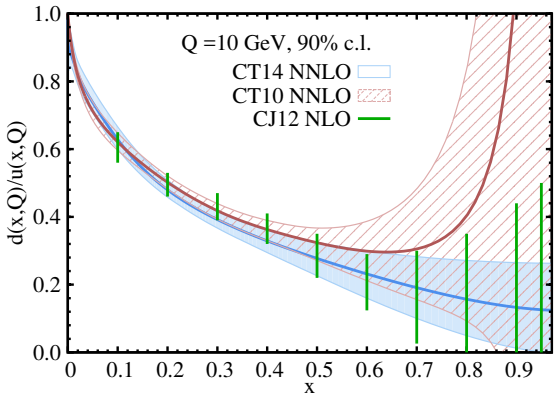

Figure 35: A comparison of 90% C.L. uncertainties on the d/u PDF ratio at $Q = 10$ GeV for CT14 NNLO (solid blue) and CT10 NNLO (dashed red), and CJ12 (green lines) error ensembles [**?**].

36. From S. Dulat, T.-J. Hou, J. Gao, M. Guzzi, J. Huston, P. Nadolsky, J. Pumplin, C. Schmidt, D. Stump, C. P. Yuan, New parton distribution functions from a global analysis of quantum chromodynamics, Phys. Rev. D93 (3) (2016) 033006

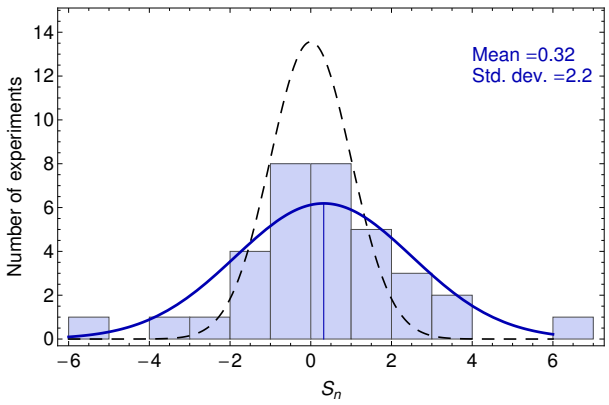

Figure 36: Best-fit values of the equivalent Gaussian variables for 33 experiments in the CT14 NNLO global analysis [**?**].

37. From S. Dulat, T.-J. Hou, J. Gao, M. Guzzi, J. Huston, P. Nadolsky, J. Pumplin, C. Schmidt, D. Stump, C. P. Yuan, New parton distribution functions from a global analysis of quantum chromodynamics, Phys. Rev. D93 (3) (2016) 033006

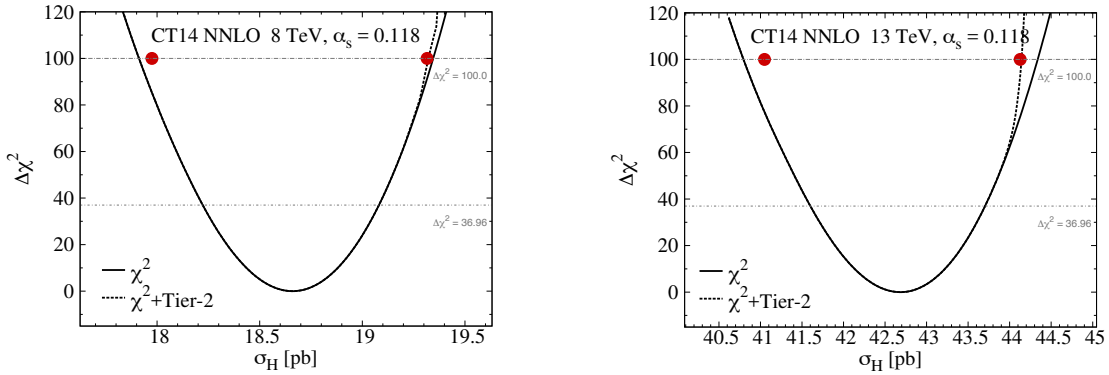

Figure 37: Dependence of the increase in χ^2 in the constrained CT14 fit on the expected cross section σ_H at the LHC 8 and 13 TeV [**?**], for $\alpha_s(M_Z)$=0.118. The solid and dashed curves are for the constrained fits without and with the Tier-2 penalties, respectively. The red dots correspond to the upper and lower 90% C.L. limits calculated by the Hessian method.

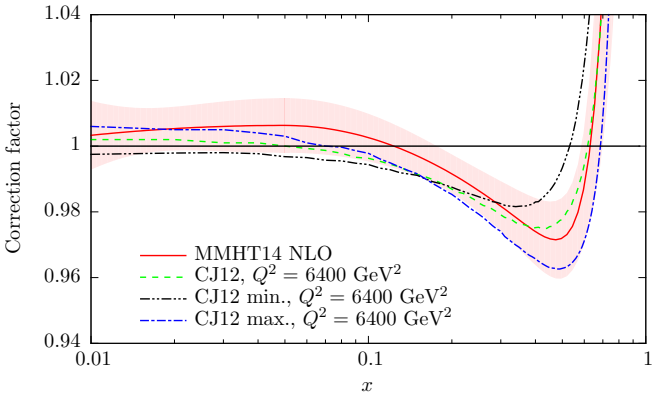

Figure 38: Fitted MMHT14 deuteron correction factors with uncertainty, compared to the CJ12 [**?**] predictions. Taken from [**?**].

38. From L. A. Harland-Lang, A. D. Martin, P. Motylinski, R. S. Thorne, Parton distributions in the LHC era: MMHT 2014 PDFs, Eur. Phys. J. C75 (5) (2015) 204. arXiv:1412.3989

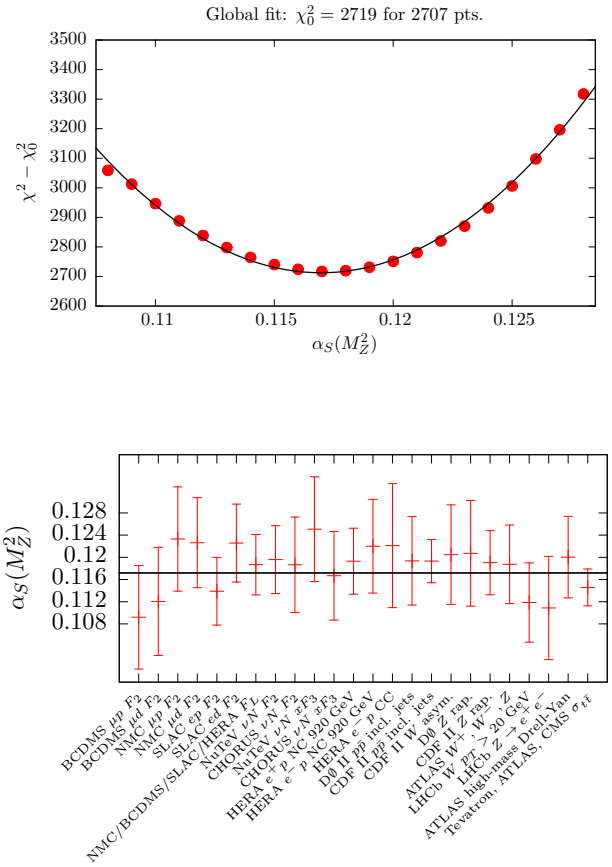

Figure 39: (Left) Global χ^2 values as a function of $\alpha_S(M_Z^2)$. (Right) Best fit $\alpha_S(M_Z^2)$ together with the upper and lower 1σ constraints from the most constraining data sets. Both figures correspond to NNLO fits and are taken from [**?**].

39. From L. A. Harland-Lang, A. D. Martin, P. Motylinski, R. S. Thorne, Uncertainties on S in the MMHT2014 global PDF analysis and implications for SM predictionsarXiv:1506.05682

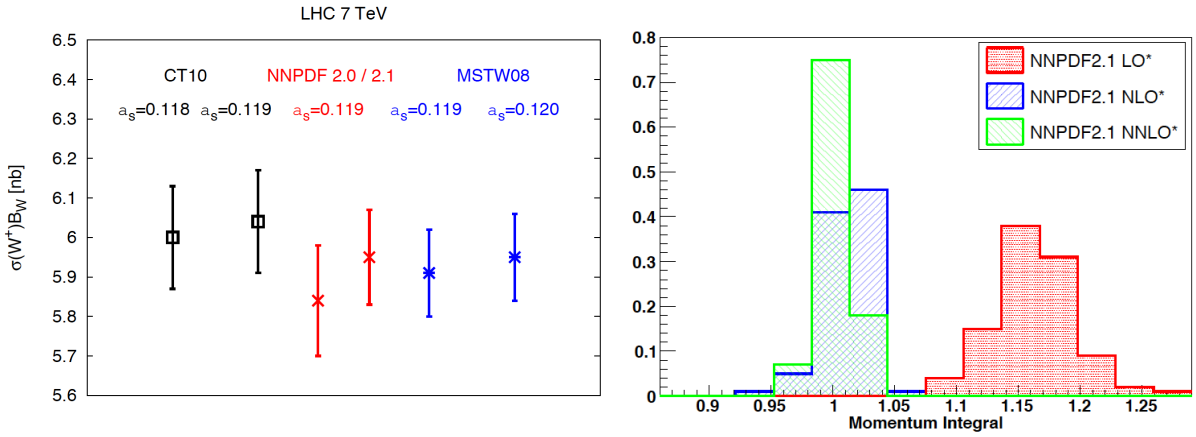

Figure 40: Left plot: comparison between the NNPDF2.0 and 2.1 predictions for the inclusive $W+$ production cross-section at the LHC 7 TeV, which illustrates the phenomenological impact of heavy quark mass effects. Right plot: the distribution of the momentum integral Eq. (**??**) among the MC replicas for the variants of the NNPDF2.1 LO, NLO and NNLO fits that do not impose explicitly the momentum sum rule.

40. From the authors

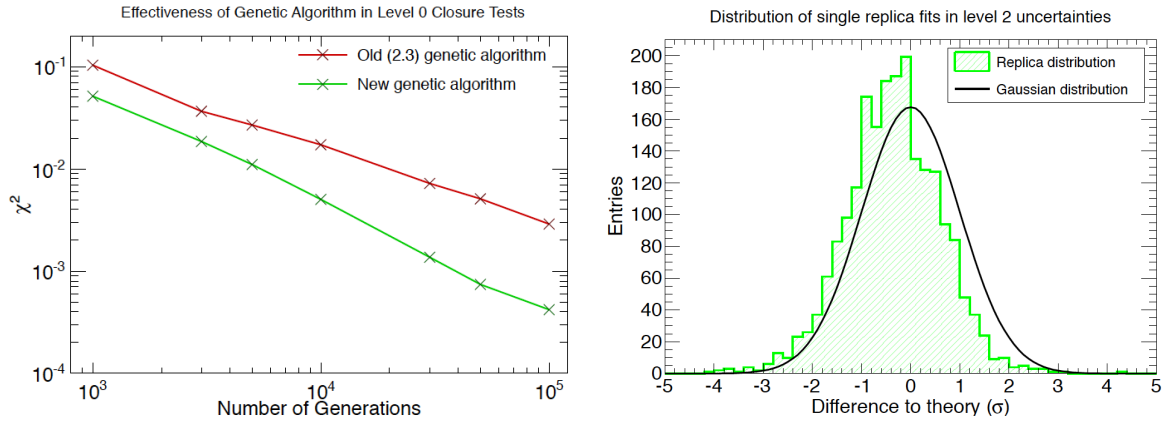

Figure 41: Representative results of the closure tests presented in the NNPDF3.0 analysis. Left plot: in a level 0 closure tests, where the pseudo-data is generated without any statistical fluctuations, the χ^2 should decrease monotonically as a function of the number of GA iterations, down to arbitrarily small values. Right plot: the distribution of the difference between theory and data in units of the error of the latter among each of the Monte Carlo replicas. This distribution is consistent with the Gaussian predicted by statistics.

41. From R. D. Ball, et al., Parton distributions for the LHC Run II, JHEP 04 (2015) 040. arXiv:1410.8849

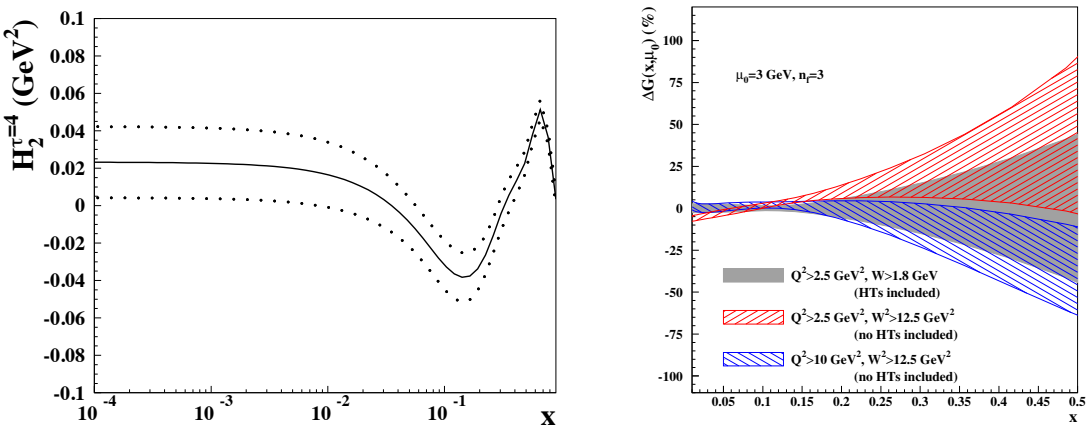

Figure 42: (Left) The higher twist coefficient for the F_2 structure function from the ABMP16 fit, including 1–σ uncertainty. (Right) Percentage difference in ABMP $n_f = 3$ gluon distribution between the default result and fits performed with higher W^2 cuts, without higher twist corrections. The 1–σ uncertainty bands are shown. Plots taken from [**?**].

42. From S. Alekhin, J. Blumlein, S. Moch, R. Placakyte, Parton Distribution Functions, s and Heavy-Quark Masses for LHC Run IIarXiv:1701.05838

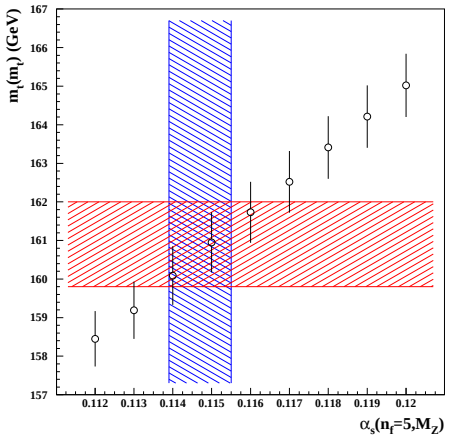

Figure 43: The $\overline{\rm MS}$ value of the top quark mass $m_t(m_t)$ obtained in the ABMP16 fit for variants of $\alpha_S(M_Z^2)$ (data points) and for the best fit values (hatched bands). Plot taken from [**?**].

43. From S. Alekhin, J. Blumlein, S. Moch, R. Placakyte, Parton Distribution Functions, s and Heavy-Quark Masses for LHC Run IIarXiv:1701.05838

44. From A. Accardi, L. T. Brady, W. Melnitchouk, J. F. Owens, N. Sato, Constraints on large-x parton distributions from new weak boson production and deep-inelastic scattering data, Phys. Rev. D93 (11) (2016) 114017. arXiv:1602.03154

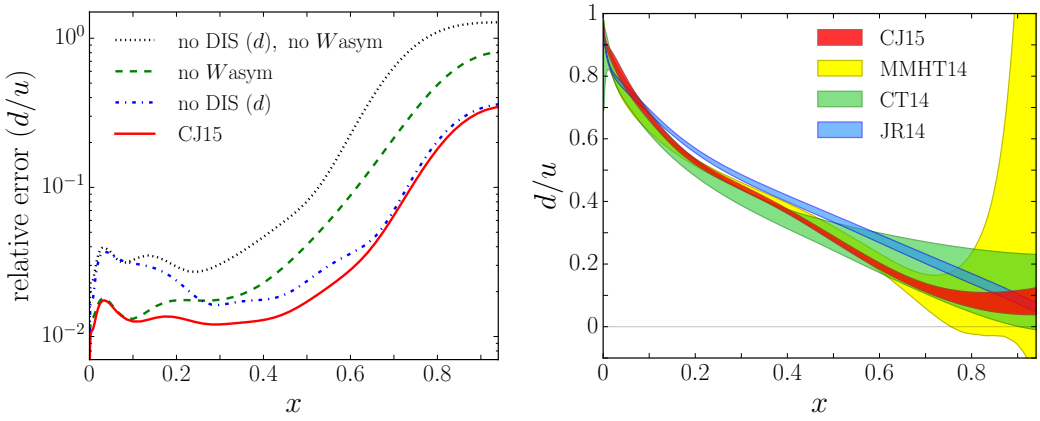

Figure 44: Left plot: relative error (90% C.L.) on the d/u PDF ratio as a function of x at $Q^2 = 10\,\mathrm{GeV}^2$ from the CJ15 fit compared with errors obtained in fits excluding certain data sets [**?**]. Right plot: comparison of the d/u ratio at $Q^2 = 10\,\mathrm{GeV}^2$ for different PDF sets, including CJ15, MMHT14, CT14, and JR14, with PDF uncertainties shown for 90% C.L. except for MMHT14 at 68% C.L. [**?**]

45. From A. Accardi, L. T. Brady, W. Melnitchouk, J. F. Owens, N. Sato, Constraints on large-x parton distributions from new weak boson production and deep-inelastic scattering data, Phys. Rev. D93 (11) (2016) 114017. arXiv:1602.03154

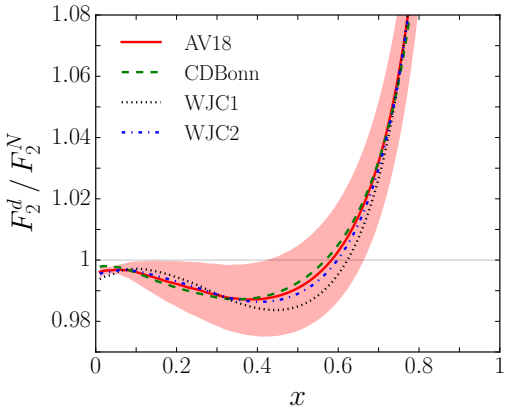

Figure 45: Ratio of deuteron to isoscalar nucleon structure functions F_2^d/F_2^N at $Q^2 = 10\,\mathrm{GeV}$ for CJ15 fits with different models of wave functions [**?**]; colored band is the 90% C.L. error for CJ15 main fit (with AV18 wave functions).

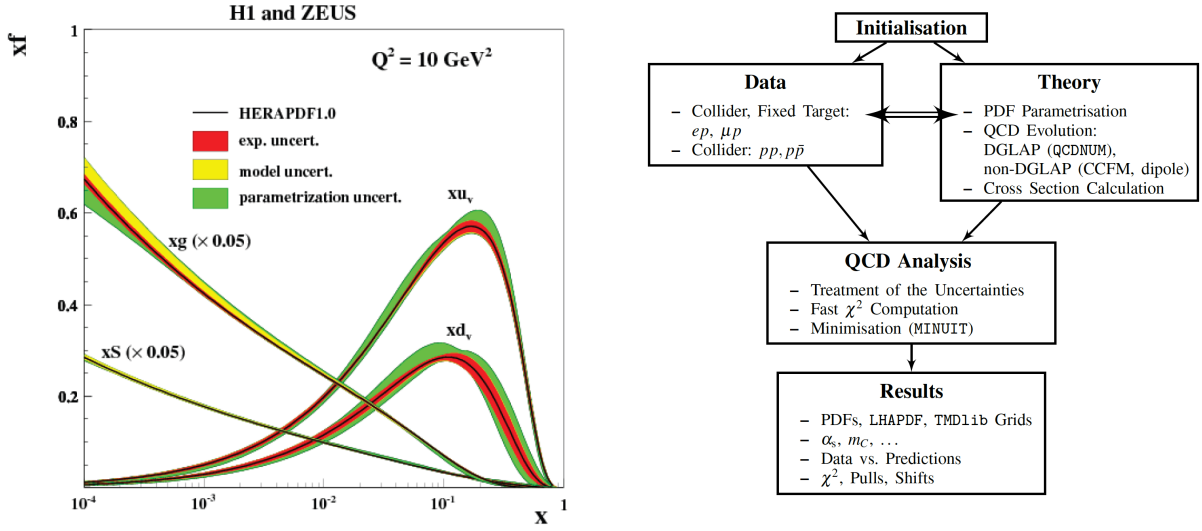

Figure 46: Left plot: the HERAPDF1.0 determination of parton distributions, based on the analysis of the combined HERA structure functions from Run I. Right plot: schematic representation of the `xFitter` code structure, see text for more details.

46. From F. Aaron, et al., Combined Measurement and QCD Analysis of the Inclusive e p Scattering Cross Sections at HERA, JHEP 1001 (2010) 109. arXiv:0911.0884

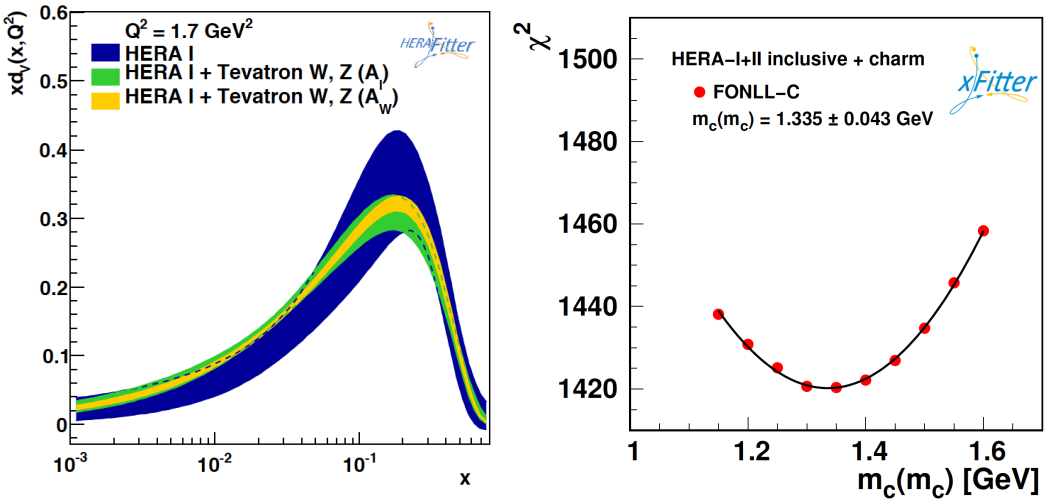

Figure 47: Two representative analyses of PDF-related studies performed by the `xFitter` Developer's Team. Left plot: the impact on d_V of the Tevatron W and Z data on a HERA-only fit, comparing the impact of the lepton-level measurements with that of the boson-level measurements, from Ref. [**?**]. Right plot: the χ^2 profile of a fit based on the inclusive HERA and charm data, as a function of the running mass $m_c(m_c)$ from Ref. [**?**]. In this analysis charm structure functions were computed with `APFEL` in the FONLL-C general mass scheme.

47. From Left: S. Camarda, et al., QCD analysis of W- and Z-boson production at Tevatron, Eur. Phys. J. C75 (9) (2015) 458. arXiv:1503.05221; Right: V. Bertone, et al., A determination of mc(mc) from HERA data using a matched heavy-flavor scheme, JHEP 08 (2016) 050. arXiv:1605.01946

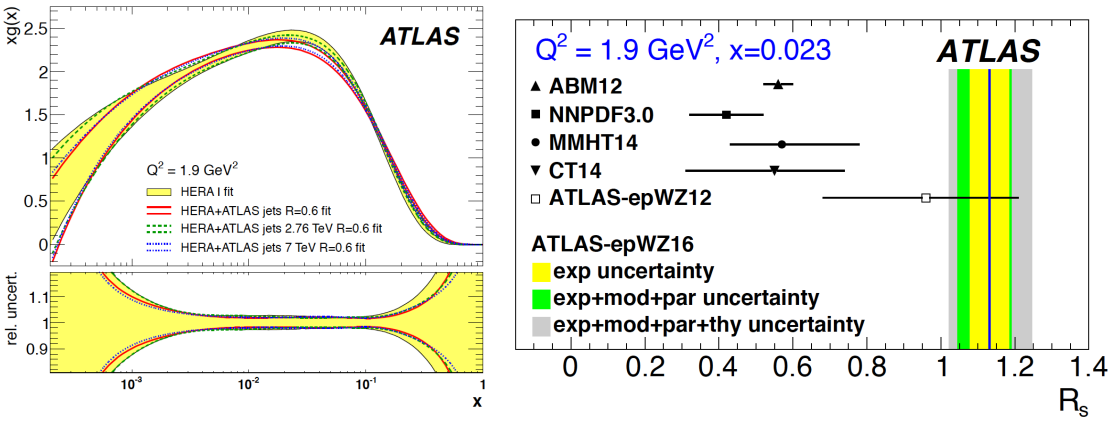

Figure 48: Two representative results of the PDF fitting efforts performed within the ATLAS collaboration. Left plot: a PDF fit quantifying the effect on the gluon from the HERA-only fit of the ATLAS inclusive jet measurements at $\sqrt{s} = 2.76$ TeV and 7 TeV, from Ref. [**?**]. Right plot: the determination of the strangeness ratio $R_s(x = 0.023, Q^2 = 1.9\,\mathrm{GeV}^2)$ for a fit to HERA data and the 2011 ATLAS measurements of the $W^{\pm}$ and Z rapidity distributions at 7 TeV, where the results of the `xFitter` analysis, denoted by ATLAS-epWZ16, are compared with the predictions from various PDF fits.

48. From Left: G. Aad, et al., Measurement of the inclusive jet cross section in pp collisions at s=2.76 TeV and comparison to the inclusive jet cross section at s=7 TeV using the ATLAS detector, Eur.Phys.J. C73 (2013) 2509; Right: M. Aaboud, et al., Precision measurement and interpretation of inclusive W+, W and Z/ production cross sections with the ATLAS detectorarXiv:1612.03016

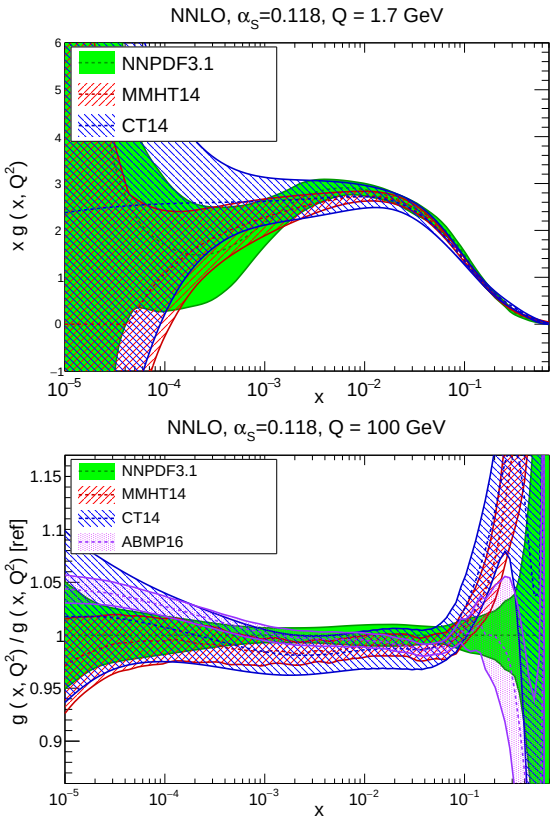

Figure 49: The gluon PDF $xg(x, Q^2)$ at $Q = 1.7$ GeV (left) and $Q = 100$ GeV (right) comparing the ABMP16, CT14, MMHT14, and NNPDF3.1 NNLO sets with $\alpha_S(m_Z) = 0.118$. In the right plots, results are normalized to the central value of NNPDF3.1.

49. From

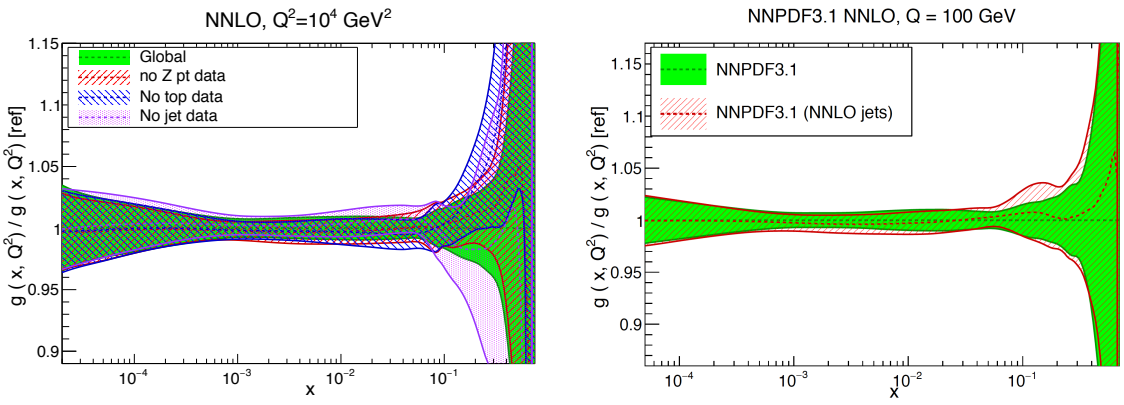

Figure 50: Left: comparison of the NNPDF3.1 NNLO global fit at $Q = 100$ GeV with the corresponding fits where the Z p_T, top quark, or inclusive jet data have been removed. Right plot: same as before, now comparing with the NNPDF3.1 NNLO fit where the ATLAS and CMS 7 TeV inclusive jet data have been treated using exact NNLO theory.

50. From

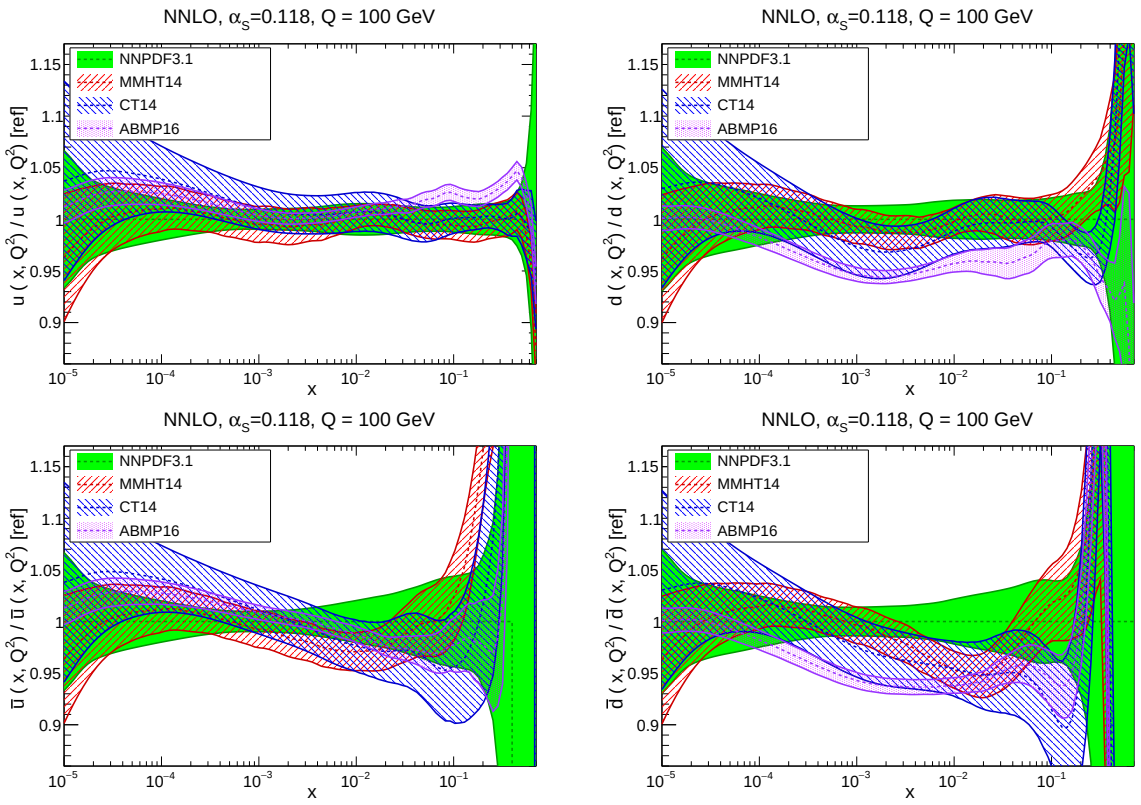

Figure 51: Same as Fig. 49 (right), now comparing the up, down, anti-up, and anti-down quark PDFs.

51. From

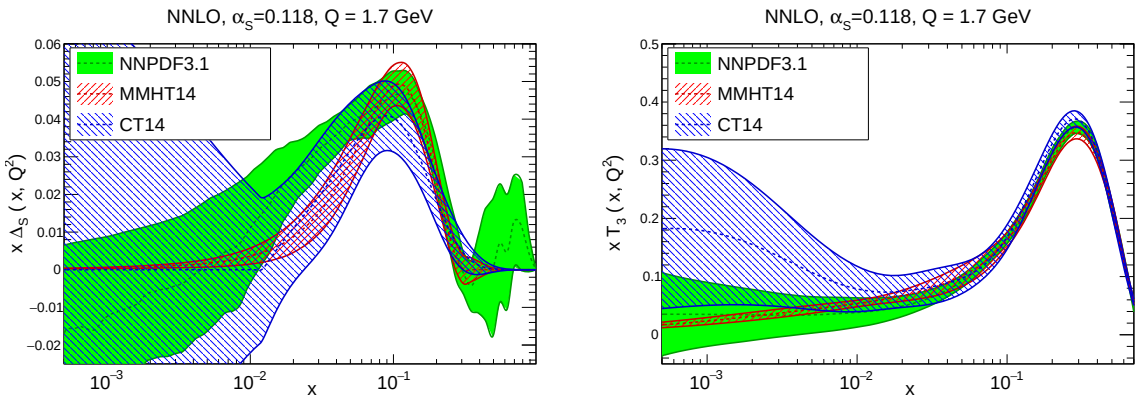

Figure 52: Same as Fig. 49 (left), now comparing the sea quark asymmetry $\Delta_S = \bar{d} - \bar{u}$ (left) and the quark isotriplet $T_3 = u + \bar{u} - d - \bar{d}$ (right plot).

52. From

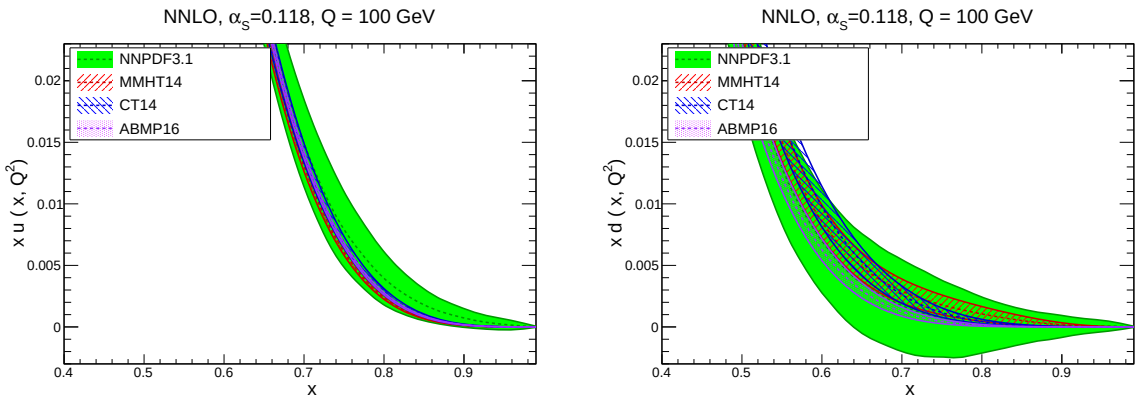

Figure 53: Same as Fig. 51, now focusing on the large-x region of the up quark (left) and down quark (right plot) PDFs.

53. From

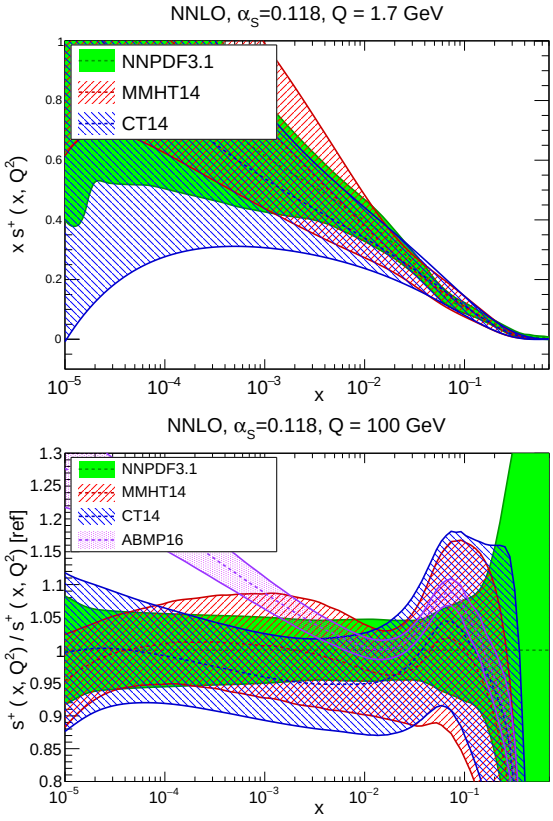

Figure 54: Same as Fig. 49 for the total strangeness $xs^+(x, Q^2)$.

54. From

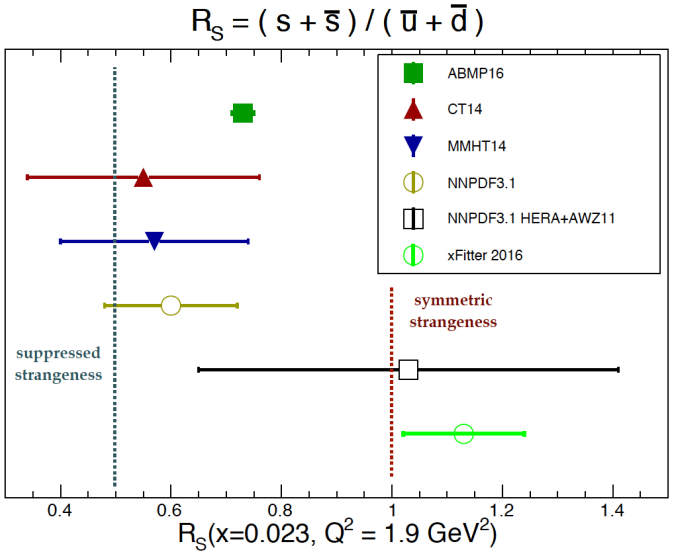

Figure 55: The ratio of strange to non-strange sea quarks $R_s(x, Q^2)$, Eq. (**??**) for $x = 0.023$ and $Q^2 = 1.9$ GeV^2. We compare the results of various global PDF fits with those of the ATLAS/`xFitter` interpretation study as well as with those of a NNPDF3.1 fit based on the same dataset as the ATLAS study. The vertical lines indicate two possible scenarios for the strange PDFs, namely a suppression of size $R_s \simeq 0.5$ and then a strange sea which is symmetric with the non-strange one, $R_S \simeq 1$.

55. From

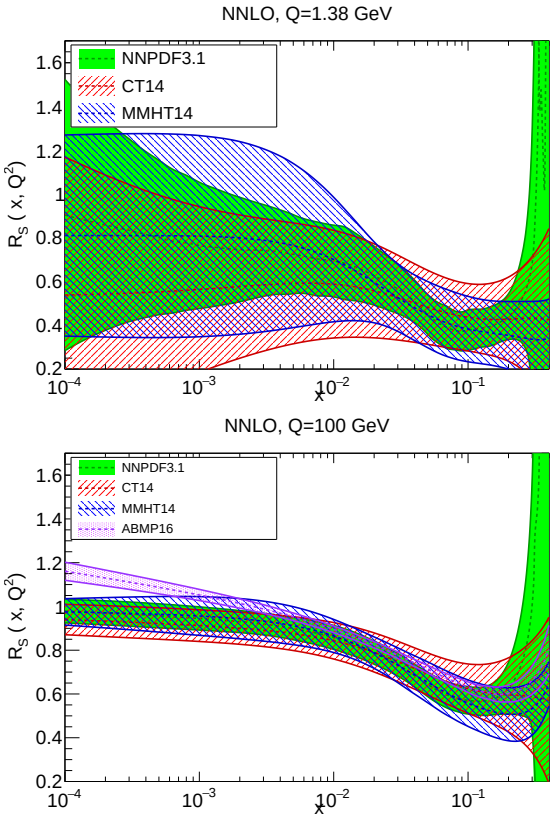

Figure 56: The ratio of strange to non-strange sea quarks $R_s(x, Q^2)$, Eq. (**??**), as a function of x for $Q = 1.38$ GeV (left plot) and for $Q = 100$ GeV (right plot).

56. From

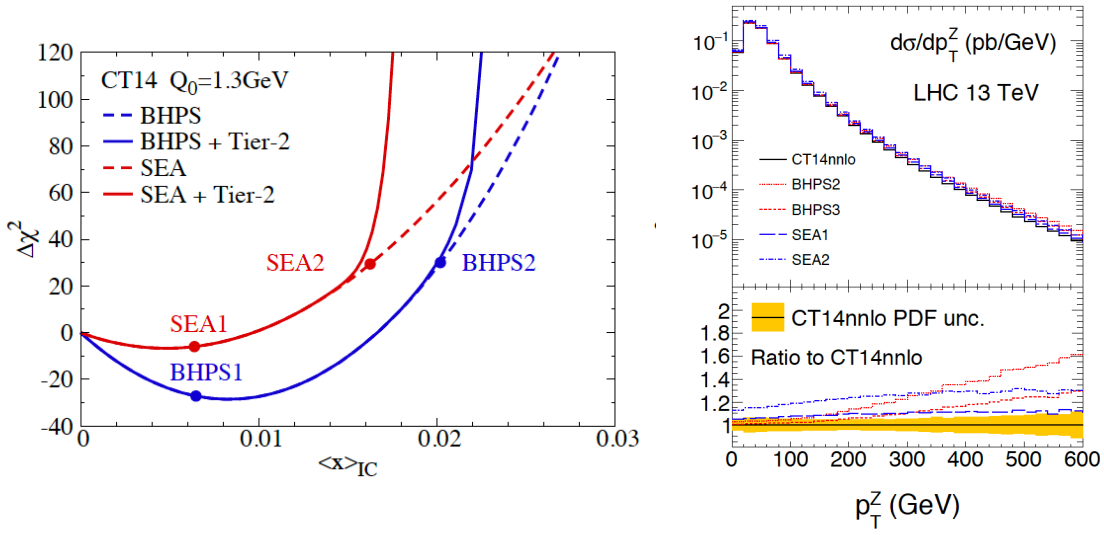

Figure 57: Left: the deviation of the χ^2 in the CT14IC fits, with respect to the best-fit value of the CT14 fit with perturbative charm, as a function of $\langle x \rangle_{\rm IC}$ Results are shown for the BHPS and SEA models, with the "1" points labeling the preferred value of $\langle x \rangle_{\rm IC}$, with those labelled with "2" indicate the largest values of the charm momentum fraction allowed by the fit tolerance criteria. Right: the transverse momentum distribution of Z bosons in the $pp \to Z + c$ process at 13 TeV, comparing the CT14 NNLO result with various of the CT14 IC models, as a function of p_T^Z.

57. From

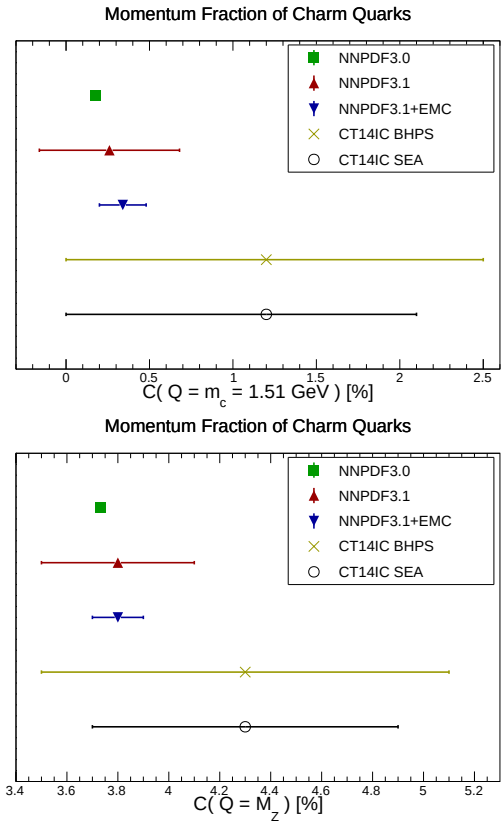

Figure 58: The momentum fraction carried by charm quarks, $C(Q)$ Eq. (**??**), both at a low scale $Q = 1.51$ GeV (left) and at a high scale $Q = M_Z$ (right plot). We compare NNPDF3.0 (perturbative charm) with NNPDF3.1 (based on fitted charm) with and without the inclusion of the EMC charm data, as well as with the BHPS and SEA scenarios of the CT14IC fits. See text for more details.

58. From

59. From

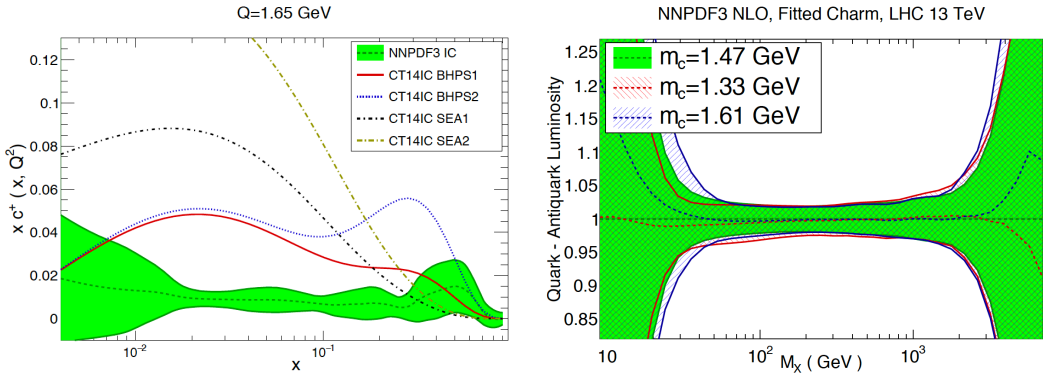

Figure 59: Left: comparison of the fitted charm PDF at $Q = 1.65$ GeV between the NNPDF3IC set and the different models of the CT14IC analysis. Right: the dependence of the quark-antiquark PDF luminosity at the LHC 13 TeV in the NNPDF3IC fits with the value of the charm mass m_c used in the fit.

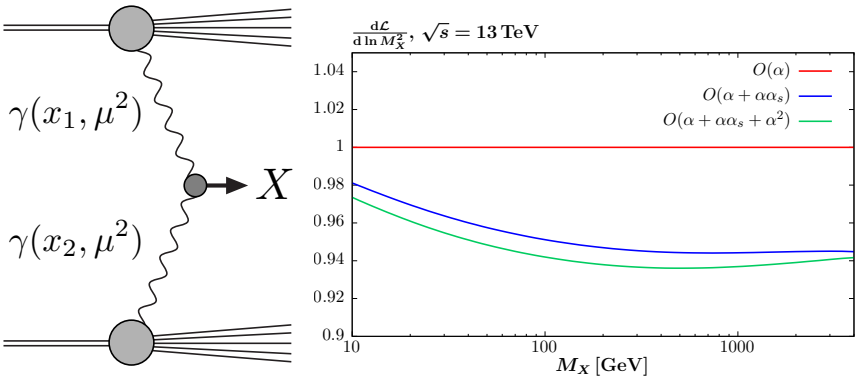

Figure 60: Left: schematic diagram for the photon–initiated production of a system X, and the corresponding photon PDFs. Right: the $\gamma\gamma$ luminosity as a function of the invariant mass, M_X, of the produced final-state, taken from [**?**]. The ratio to results with $O(\alpha\alpha_S)$ and $O(\alpha^2)$ to the leading $O(\alpha)$ DGLAP evolution shown.

60. From

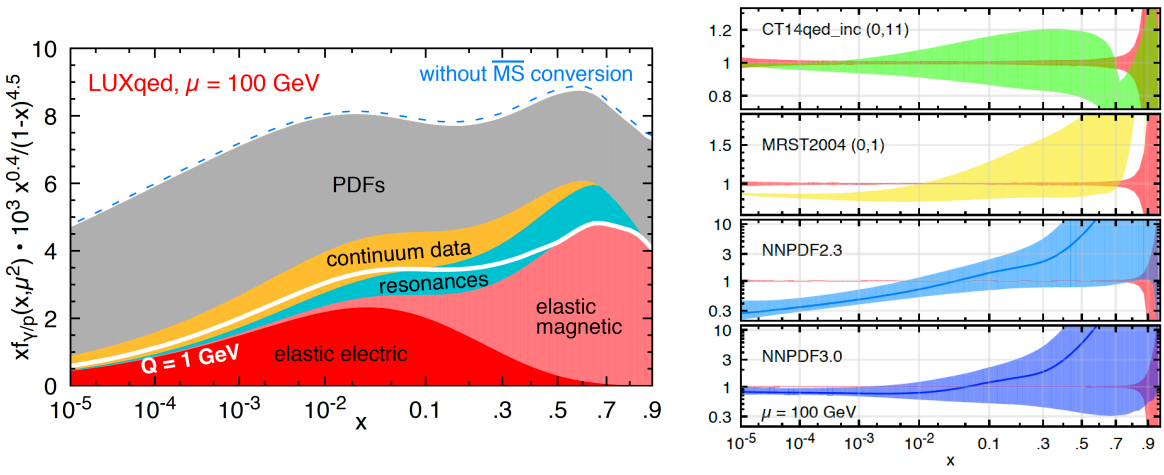

Figure 61: Left: overview of the various contributions to the photon PDF $\gamma(x, Q^2)$ in the LUXqed approach as a function of x at $Q = 100$ GeV. Right: comparison of the photon PDFs from CT14qed_inc, MRST2004, NNPDF2.3/3.0 and LUXqed, normalized to the central value of the latter.

61. From

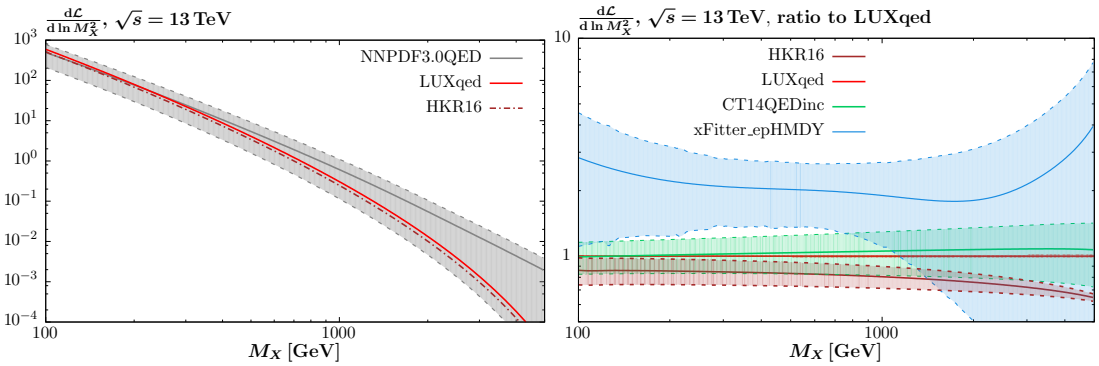

Figure 62: $\gamma\gamma$ luminosities at $\sqrt{s} = 13$ TeV. (Left) Absolute values for the HKR16, NNPDF3.0QED and LUXqed sets. (Right) Ratios of the CT14QED, HKR16 and `xFitter_HMDYep` sets to the LUXqed prediction. 68% uncertainty bands are shown, with the exception of the HKR16 set, where the error is due to model variation in the inelastic input (lower edge corresponds to elastic only).

62. From

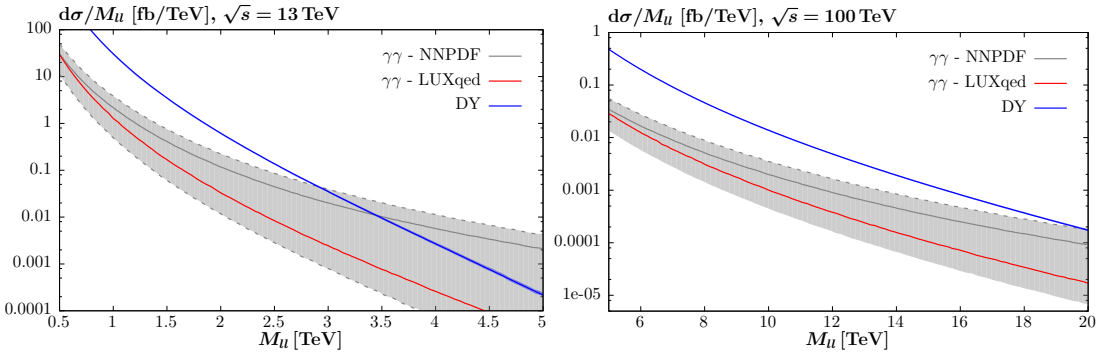

Figure 63: The differential lepton pair production cross sections at $\sqrt{s} = 13$ TeV and 100 TeV with respect to the invariant mass of the pair M_{ll}, for lepton $|\eta| < 2.5$ and $p_\perp > 20$ GeV. The photon–initiated contributions predicted using the LUXqed and NNPDF3.0QED sets, including the 68% C.L. uncertainty bands. The NLO Drell–Yan cross section, calculated with `MCFM` [**?**], is also shown.

63. From

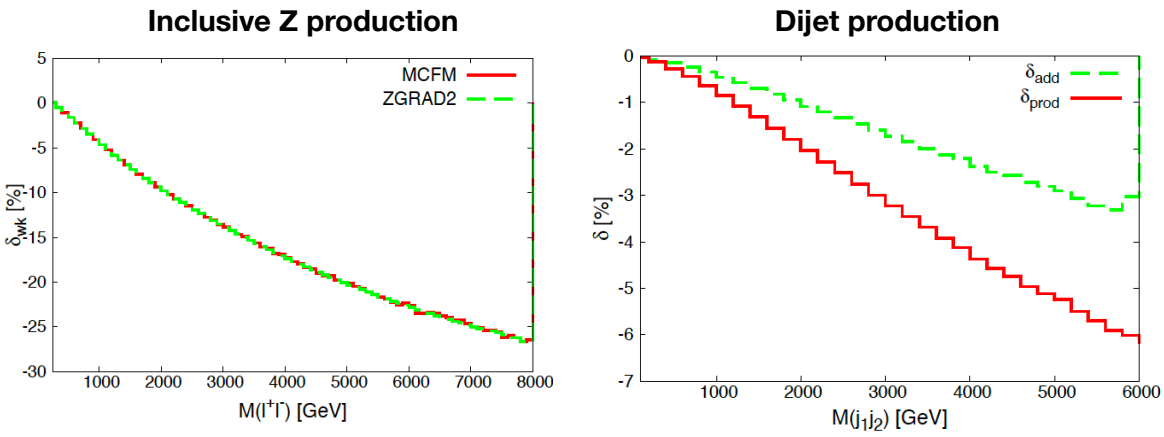

Figure 64: Two representative examples of NLO EW corrections for processes relevant for PDF determinations, computed with MCFM at $\sqrt{s} = 13$ TeV [**?**]. In the left plot, we show the percentage NLO EW correction for high-mass dilepton production as a function of M_{ll}, comparing also with the corresponding ZGRAD calculation. In the right plot, we show the same quantity, now for dijet production as a function of the invariant mass of the dijet M_{jj}. The two curves correspond to two possible ways to combine NLO QCD and EW corrections, known as additive ($\delta_{\rm add}$) and multiplicative ($\delta_{\rm prod}$).

64. From

65. From

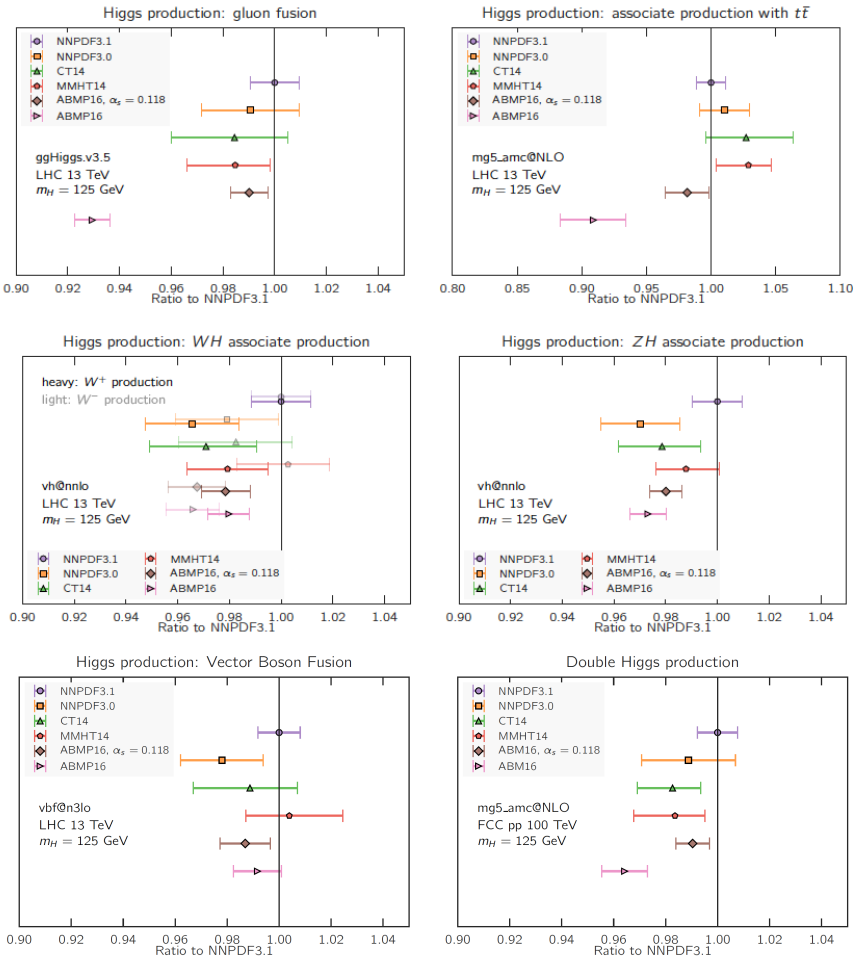

Figure 65: The PDF dependence of the most important Higgs production inclusive cross-sections at the LHC 13 TeV. The results are normalized to the central value of NNPDF3.1, and only PDF uncertainties are shown. See text for more details of the theoretical calculation.

66. From

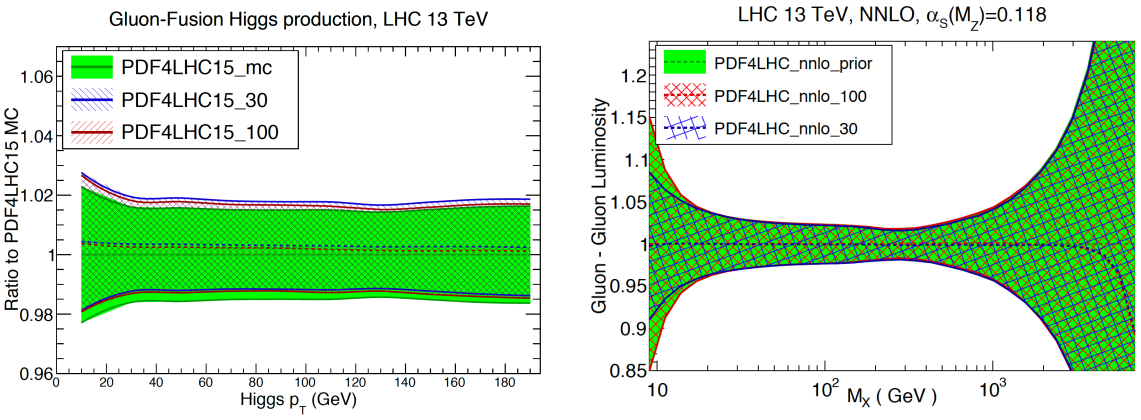

Figure 66: Left: the PDF uncertainties in the p_T^h distribution of Higgs bosons produced in the gluon-fusion mode at the LHC 13 TeV for $0 \leq p_T^h \leq 200$ GeV, computed using the PDF4LHC15 sets. Right: the gluon-gluon PDF luminosity with the same set now extending up to higher values of the invariant mass of the final state M_X.

67. From

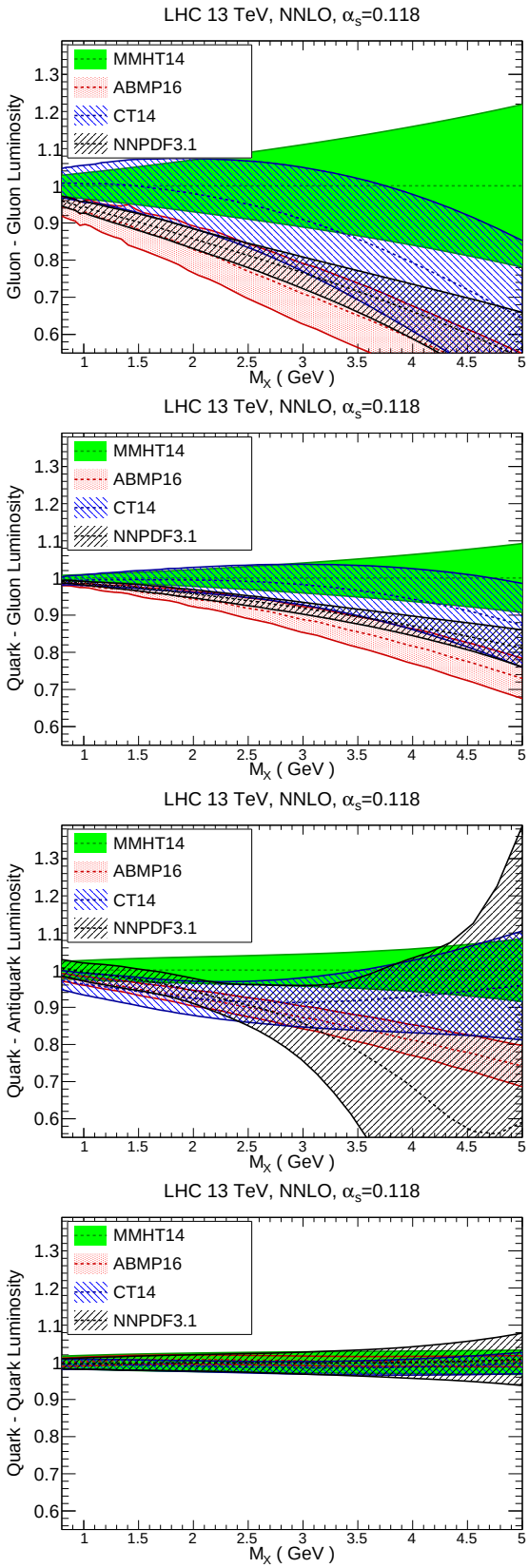

Figure 67: Comparison of PDF luminosities in the large invariant mass M_X region between MMHT14, ABMP16, CT14 and NNPDF3.1. From left to right and from top to bottom we show the results of the gluon-gluon, gluon-quark, quark-antiquark and quark-quark luminosities, normalized to the central value of MMHT14. In this comparison, NNLO PDFs with $\alpha_s(m_Z) = 0.118$ sets are used.

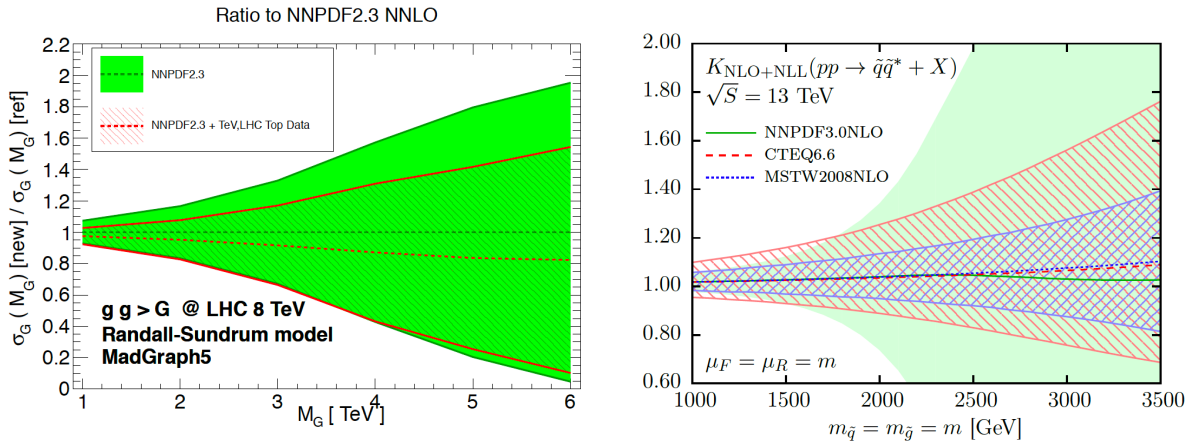

Figure 68: Left: the PDF uncertainties for high-mass graviton production in the Randall-Sundrum scenario induced by gluon-fusion at the LHC 8 TeV, computed with `MadGraph5`. We compare the results of the NNPDF2.3 fit with that of the same fit including the constraints from top-quark production cross-sections. Right: the K-factor for the NLO+NLL cross-section, including PDF uncertainties, for the production of a squark-anti-squark pair $\tilde{q}\tilde{q}^*$ at the LHC 13 TeV with various PDF sets.

68. From

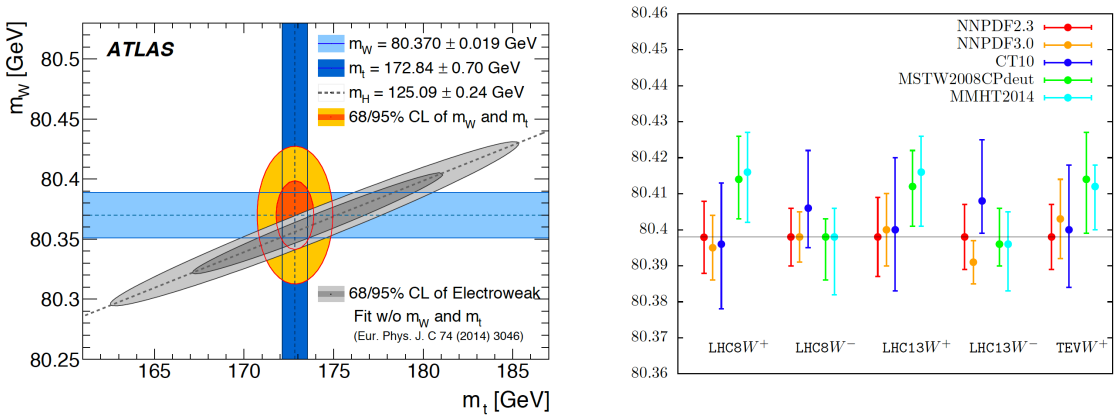

Figure 69: Left: comparison of the direct measurements of m_W, m_t, and m_h from ATLAS with the predictions from the global electroweak fit, from [**?**]. Right: estimate of the PDF uncertainties in the m_W determination using different PDF sets and collider scenarios, from [**?**] This estimate has been obtained from template fits to the p_T^l distribution, imposing the constraint that $p_T^W \leq 15$ GeV.

69. From

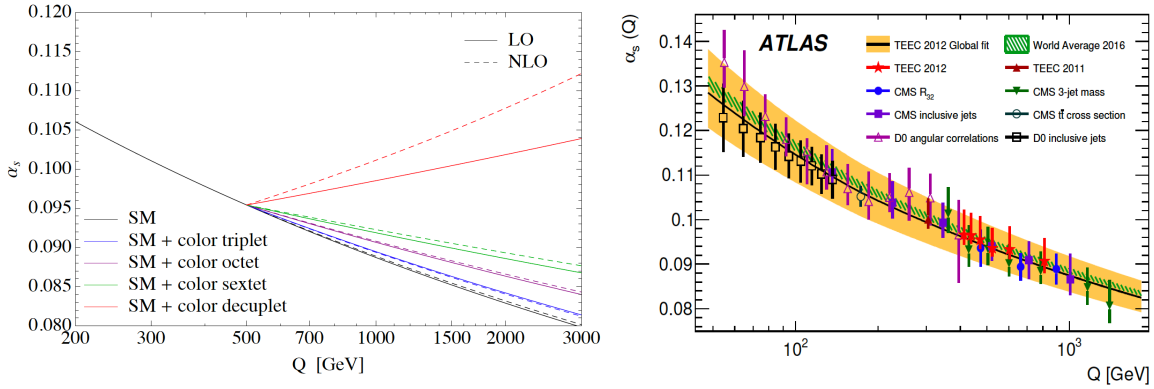

Figure 70: Left: the modification in the running of $\alpha_s(Q)$ induced by a new heavy colored fermion of mass $m = 0.5$ TeV as compared to the SM prediction, for various representations of its color gauge group, from [**?**]. Right: comparison of recent direct determinations of $\alpha_s(Q)$ at the Tevatron and the LHC as a function of Q, together with the PDG 2016 world average and with the results of the global ATLAS TEEC 2012 fit.

70. From

71. From

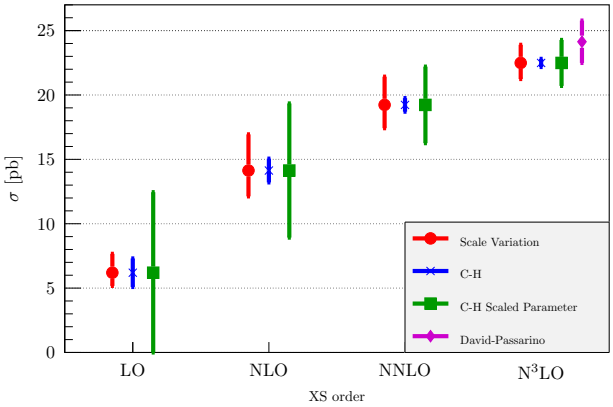

Figure 71: The cross section for Higgs production in gluon fusion calculated at increasing perturbative orders [**?**]. At each order the theoretical uncertainty is shown for using scale variation (red circles), the CH method (blue crosses), and the $\overline{\text{CH}}$ method (green squares); at N^3LO the Passarino-David uncertainty based on series acceleration method is also shown (purple diamonds).

72. From

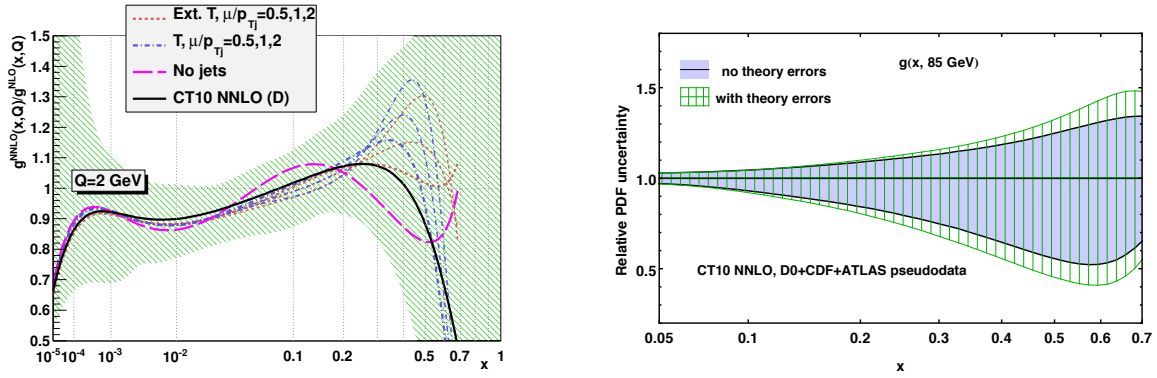

Figure 72: Left plot: dependence of the gluon PDFs on the choice of QCD scales in calculation of inclusive jet cross sections in CT10 NNLO fits [**?**]. Right plot: impact of the theoretical uncertainties of inclusive jet cross sections on the gluon PDFs in CT10 NNLO fits [**?**] .

73. From

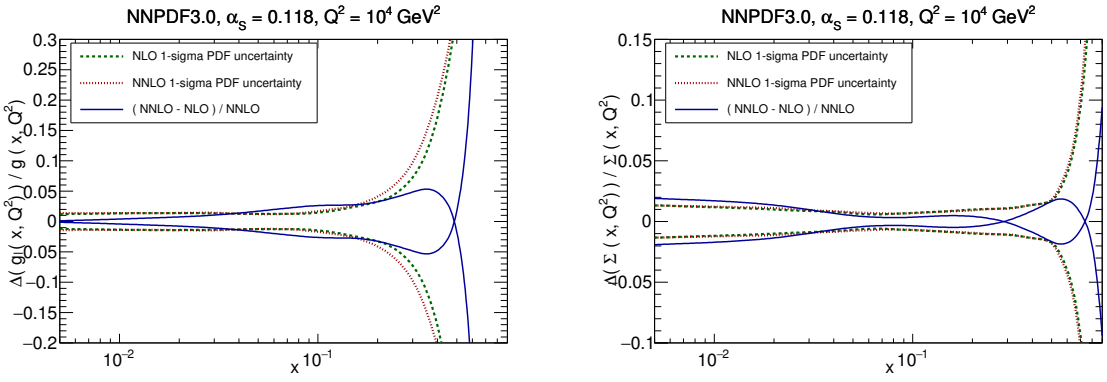

Figure 73: Left(right) plot shows comparisons between the conventional PDF uncertainties and the differences of the central PDFs determined at NLO and NNLO for the gluon(total singlet) PDF as from NNPDF3.0 [**?**].

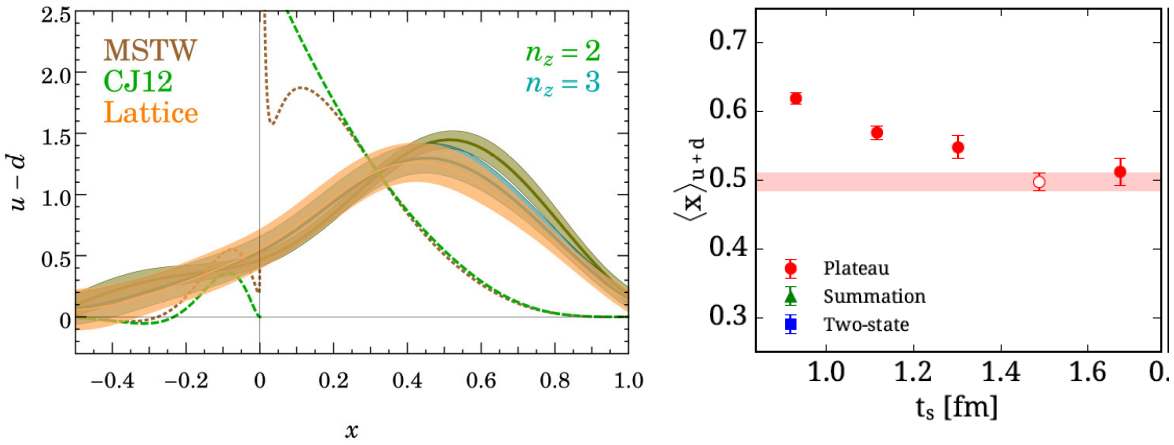

Figure 74: Left plot: the $u(x) - d(x)$ difference as a function of Bjorken x, where the results of a recent lattice QCD calculation based on quasi-PDFs is compared with the MSTW08 and CJ12 results. Right plot: the momentum fraction carried by sum of up and down quarks, $\langle x \rangle_{u+d}$ for different values of the parameter t_s (points with errors), compared with the results from recent global PDF fits (horizontal band).

74. From

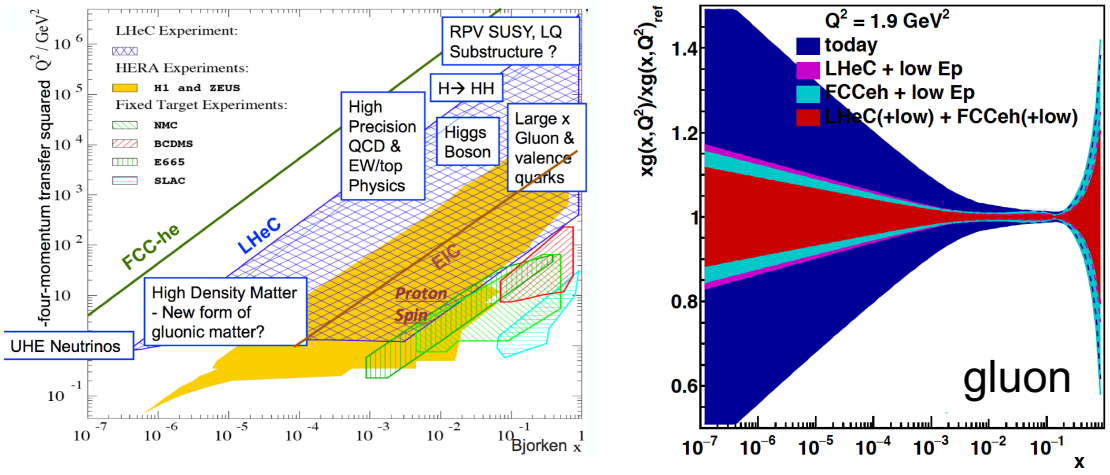

Figure 75: Left plot: kinematic coverage in the (x, Q^2) of several existing and proposed deep-inelastic scattering experiments. Starting from the fixed-target experiments and then moving to HERA, the LHeC and finally the FCC-eh, as the center of mass energy increases, the kinematic reach extends both towards higher Q^2 and smaller x values. Right plot: results of an `xFitter` PDF feasibility study that compares the impact on the gluon PDF of adding either LHeC or FCC-eh (or both) pseudo-data in addition to the HERA inclusive structure function dataset.

75. From

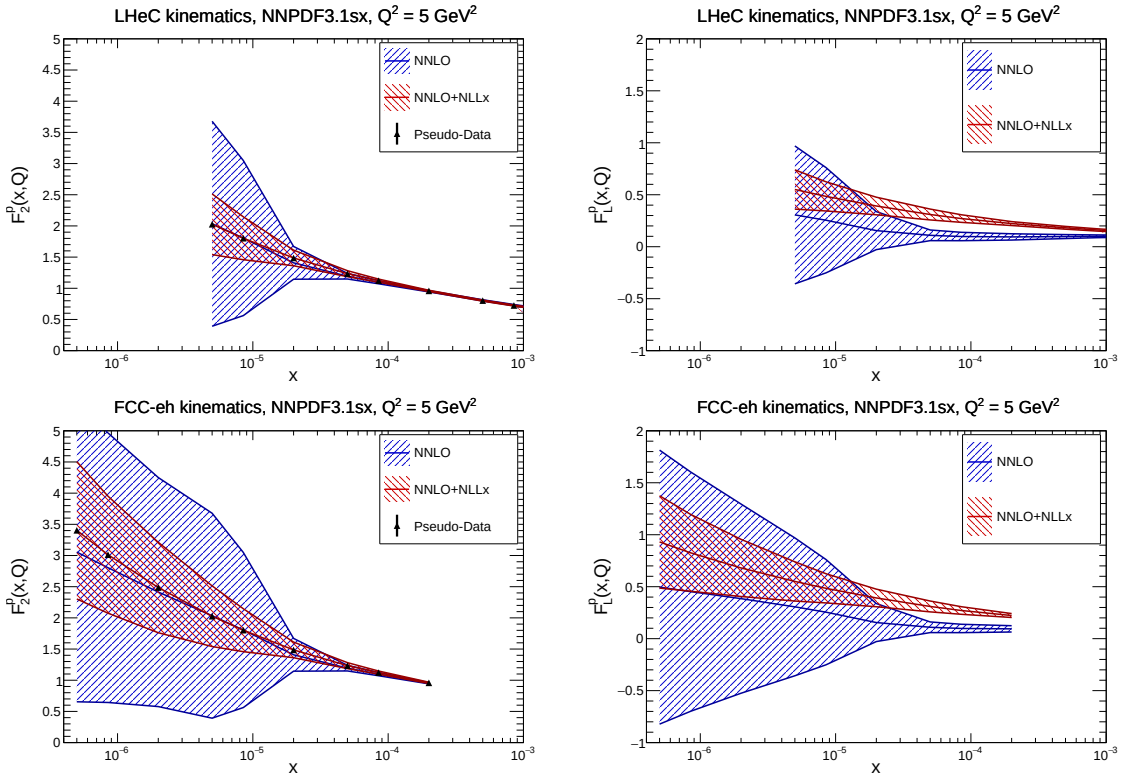

Figure 76: The theoretical predictions for the F_2 and F_L structure functions at the LHeC (upper) and FCC-eh (lower plots) using the NNPDF3.1sx NNLO and NNLO+NLLx fits at $Q^2 = 5$ GeV^2. In the case of the F_2^p structure function, we also show the expected total experimental uncertainties based on the simulated pseudo-data, assuming the NNLO+NLLx values as central prediction.

76. From

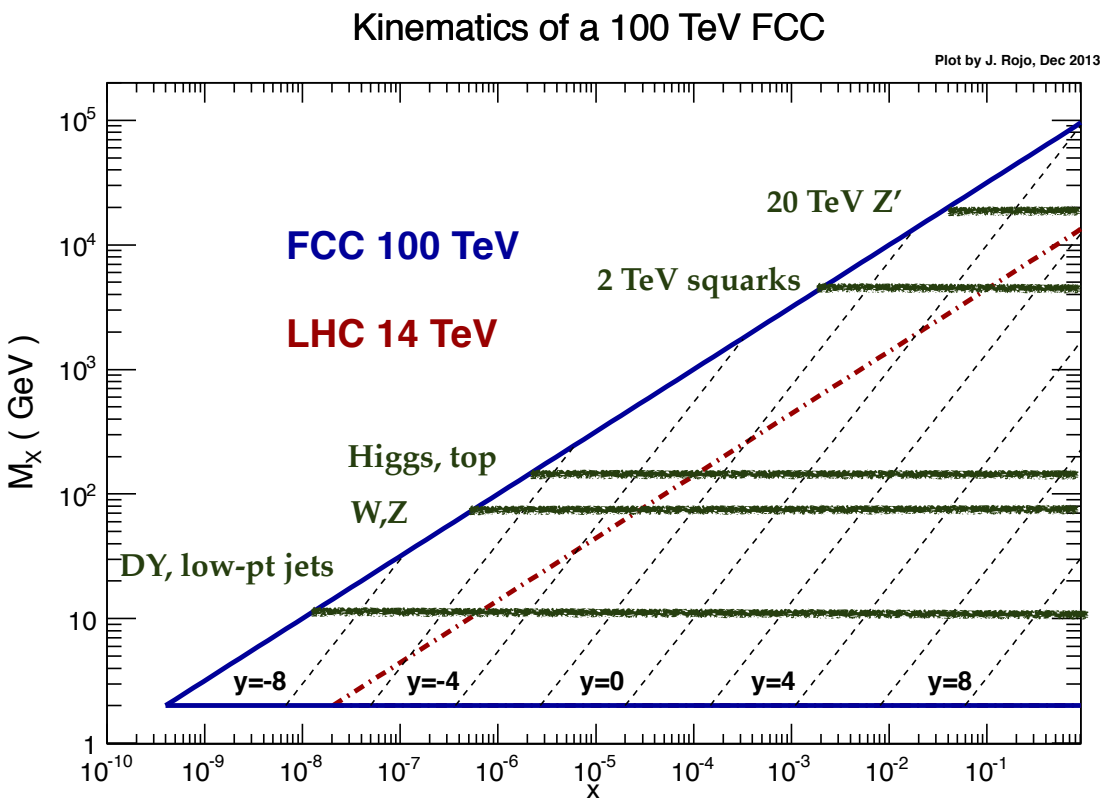

Figure 77: Kinematic coverage in the (x, M_X) plane of a $\sqrt{s} = 100$ TeV hadron collider (solid blue line), compared with the corresponding coverage of the LHC at $\sqrt{s} = 14$ TeV (dot-dashed red line).

77. From

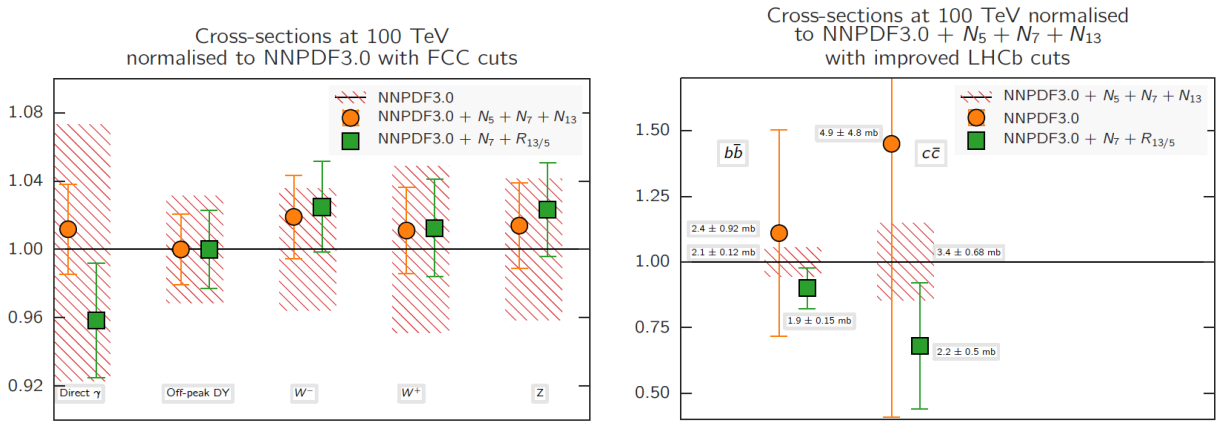

Figure 78: Comparison of cross-sections for different representative processes at the FCC with $\sqrt{s} = 100$ TeV, between the NNPDF3.0 predictions and those of the NNPDF3.0+LHCb sets, as discussed in the text. The acceptance cuts are different in each process. In the left plot we show the results for direct photon production, off-peak Drell-Yan cross-sections, and inclusive weak boson production. In the right plot we show the fiducial cross-sections for $c\bar{c}$ and $b\bar{b}$ production.

78. From

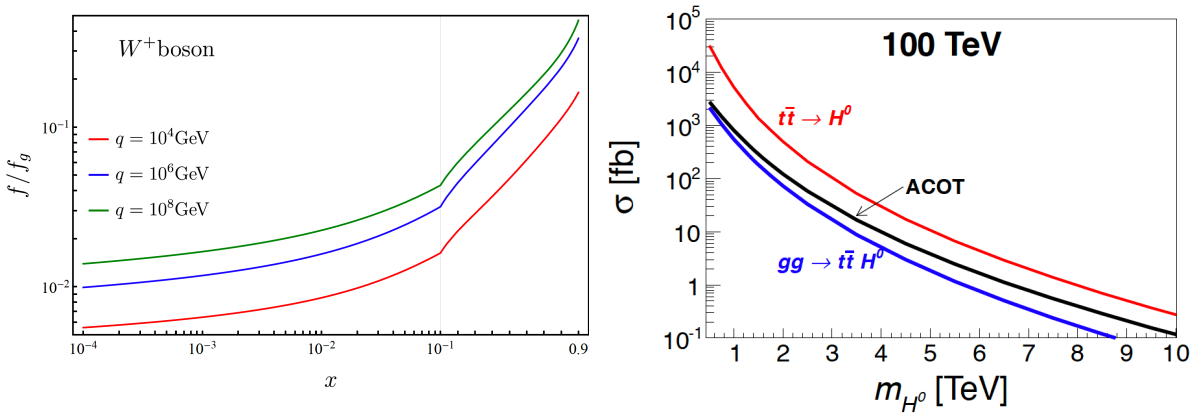

Figure 79: Left: the PDF of the W^+ boson normalized to that of the gluon, as a function of x for different scales: $q = 10^4$ GeV, 10^6 GeV, 10^8 GeV, from Ref. [**?**]. Right: the cross-section inclusive Higgs production by $t\bar{t}$ associated production, comparing the results of the $n_f = 5$ scheme ($gg \to ht\bar{t}$), the $n_f = 6$ scheme ($t\bar{t} \to h$), and of their interpolation by means of the ACOT general-mass scheme.

79. From